Frictional losses in a bubbling fluidized bed with horizontal flow of solids

Citation for the original published paper (version of record):
Farha, M., Guio Perez, D., Johnsson, F. et al (2025). Frictional losses in a bubbling fluidized bed with horizontal flow of solids. International Journal of Multiphase Flow, 189.
http://dx.doi.org/10.1016/j.ijmultiphaseflow.2025.105192

International Journal of Multiphase Flow 189 (2025) 105192

Contents lists available at ScienceDirect

International Journal of Multiphase Flow

journal homepage: www.elsevier.com/locate/ijmulflow

Research Paper

Frictional losses in a bubbling fluidized bed with horizontal flow of solids

Munavara Farha [*], Diana Carolina Guío-Pérez, Filip Johnsson, David Pallarès

Chalmers University of Technology, Hörsalsvägen 7B, 412 96 Gothenburg, Sweden

A R T I C L E I N F O

Keywords:
Bubbling fluidized bed
Fluid-dynamical scaling
Solids crossflow
Solids convection
Frictional losses
Magnetic solids tracing

A B S T R A C T

This study investigates the frictional losses in a horizontal flow of solids fluidized under bubbling conditions, relevant to applications like combustion, gasification, drying, and waste incineration. Experiments were conducted in a fluid-dynamically down-scaled setup simulating a bed of Geldart type B solids, fluidized under typical industrial conditions for thermochemical conversion processes, corresponding to sand (particle density: 2650 kg/m^3; diameter: 950 μm) fluidized with air/flue gas at 900 °C. The rig features a bubbling bed with a closed horizontal loop for controlled solids circulation, equipped with in-bed pressure probes to measure horizontal pressure drop. Horizontal solids velocity was evaluated by performing magnetic solids tracing experiments. Key parameters varied included solids velocity (0–0.10 m/s), channel width (0.58–1.0 m), and settled bed height (0.67–0.83 m).

The results clearly indicate a horizontal pressure gradient (15–485 Pa/m), which is proportional to the solids' mean velocity (0–0.101 m/s in upscaled terms). An inverse relationship between the pressure gradient and channel width was also identified. Rheological analysis indicates shear-thinning behavior, with wall shear stress ranging from 10 to 140 Pa for shear rates of 2×10^{-3}–0.45 s^{-1} (on an up-scaled basis). Existing models for non-Newtonian flow were found to underestimate the impact of geometric parameters. An alternative correlation is proposed, and friction coefficients are calculated. Analysis of friction coefficients against the Reynolds number confirms laminar flow. Additionally, a strong positive correlation between the generalized Reynolds and Péclet numbers highlights the impact of viscous forces in solids mixing. Lastly, the friction factor analysis, based on granular flow rheology, indicates that friction dynamics occur within the dense flow regime.

1. Introduction

The establishment of a horizontal solids flow in a bubbling fluidized bed is a desirable feature that finds use in various fluidized bed applications, particularly in processes that are of importance for the energy sector's transition towards sustainability. These include dual fluidized bed systems, such as those used in biomass gasification, chemical looping processes (combustion, gasification, cracking), and thermochemical energy storage (Basu, 2006; Winter and Schratzer, 2013). Horizontal solids flow is also critical in operations like drying, iron ore reduction, pharmaceutical production, and waste incineration (Yates, 1983; Kunii and Levenspiel, 1991; Winter and Schratzer, 2013; Pawar et al., 2020). In all these applications, an efficient operation requires significant mass and heat transfer, which depend on the ability to circulate solids.

In contrast to vertical transport, horizontal solids flow demonstrates a greater ability to generate plug flow-like behavior, reducing back-mixing (Wanjari et al., 2006; Levenspiel, 2012; Chen et al., 2017). This flow pattern is particularly beneficial for processes requiring narrow residence time distributions, such as biomass gasification and chemical looping (Murakami et al., 2007; Aronsson et al., 2017). Similarly, in drying and pharmaceutical production, a homogeneous and controllable residence time distribution ensures uniform exposure to heat and reactants, which is crucial for product quality and process control (Ramli and Daud, 2007; Kong et al., 2018; Zhang and Abatzoglou, 2022). In iron ore reduction and waste incineration, this flow pattern also helps prevent local overheating or incomplete reactions, facilitating temperature control and reaction uniformity (Yin et al., 2008; Parvathaneni et al., 2024). Furthermore, horizontal convection of a dense bed allows for more compact units and lower compression requirements compared to traditional vertical solids convection.

The frictional losses incurred between the horizontally flowing bed of solids and the reactor walls, as well as between the bed solids, are key design considerations. These losses directly affect the solids flow patterns and can have major impacts on the overall energy efficiency of the operation. Since applications with horizontal flow of fluidized solids is still limited, there is a significant gap in the scientific knowledge

---

[*] Corresponding author.
E-mail address: m.farha@chalmers.se (M. Farha).

https://doi.org/10.1016/j.ijmultiphaseflow.2025.105192
Received 21 October 2024; Received in revised form 4 February 2025; Accepted 21 February 2025

Nomenclature

A	cross-sectional area [m^2]
a, b	geometrical parameters, as defined by the Kozicki et al. model [−]
C	geometrical constant [−]
C_i	concentration [kg/m^3]
C_W, C_{H_b}	geometrical parameters, as defined by the proposed model [−]
D	equivalent bed diameter [m]
D_h	hydraulic diameter [m]
D_S	solids lateral dispersion coefficient [m^2/s]
d_S	mean particle diameter [μm]
f_F	fanning friction factor [−]
g	gravity constant, 9.81 [m/s^2]
G_S	solids circulation rate [kg/m^2 s]
H	bed height [m]
H_b	expanded bed height [m]
I	inertial number [−]
I_0	constant, $\mu(I)$ constitutive law [−]
K	flow consistency index constant [Pa s^n]
k^*	flow consistency index [Pa s^n]
L	length [m]
n^*	flow behavior index [−]
P	pressure [Pa]
P_p	particle pressure [Pa]
PSD	particle size distribution [−]
Per	wetted perimeter [m]
Re^*	Reynolds number [−]
t	time [s]
u_0	fluidization velocity [m/s]
u_{mf}	minimum fluidization velocity [m/s]
u_r	relative velocity between the phases [m/s]
u_S	solids velocity [m/s]
W	channel width [m]
x	horizontal position [m]

Greek letters

β	geometrical parameter, as defined by the Delplace–Leuliet model [−]
ε_g	bed voidage [−]
ε_S	solids concentration [−]
η	apparent viscosity [Pa s]
λ	shape factor constant [−]
ρ_B	bulk density [kg/m^3]
ρ_f	density of the bed in fluidized state [kg/m^3]
ρ_g	density of gas [kg/m^3]
ρ_S	density of solid particles [kg/m^3]
$\mu(I)$	effective friction coefficient [−]
μ_2	friction coefficient at high inertial numbers, $\mu(I)$ constitutive law [−]
μ_F	gas viscosity [Pa s]
μ_S	static friction coefficient, $\mu(I)$ constitutive law [−]
ξ	geometrical parameter, as defined by the modified Kostic–Hartnett model [−]
τ_w	wall shear stress [Pa]
$\dot{\gamma}_a$	apparent shear rate [s^{-1}]
$\dot{\gamma}_w$	wall shear rate [s^{-1}]
φ	particle sphericity [−]

concerning the specifics of these frictional losses, particularly their magnitude and how they vary with different operational parameters. This lack of understanding poses substantial challenges for process design and scale-up efforts.

While not being specific to horizontal flow of solids, previous research has indeed explored methodologies for quantifying frictional losses in fluidized beds, primarily through the solids friction factor, f, which represents the relative flow resistance through the ratio of viscous to inertial forces. Numerous correlations for this factor exist in literature, mainly addressing dilute-phase flow in circulating fluidized bed (CFB) risers and pneumatic conveying systems. In these systems, differential pressure measurements are utilized to deduce the profile of average solids concentration which, combined with assumptions or measurements of the solids transport velocity, allow to estimate the solids flux (Jones et al., 1967; Konno and Saito, 1969; Capes and Nakamura, 1973; Kmieć et al., 1978; Özbelge, 1984; Hariu and Molstad, 1949; Breault and Mathur, 1989; Garić et al., 1995; Rautiainen and Sarkomaa, 1998; Lech, 2001; Jones and Williams, 2003; Mabrouk et al., 2008). However, pressure measurements often make it difficult to isolate the distinct impacts of pressure drops due to the gas-solid suspension, wall friction, and particle acceleration. There are only a few investigations into the precise delineation of these contributions, and the existing research focuses primarily on circulating fluidized bed risers. In such systems, the solids flow occurs in the vertical direction that are distinct from those in focus in the present study (bubbling beds with horizontal solids flow). Table 1 provides a summary of the correlations reported in literature pertaining to frictional pressure drops that result from particle-wall interactions. Note that in most correlations, the friction factor is a function of the solids' velocity 'u_S'.

As indicated above in Table 1, solids friction factor correlations predominantly rely on empirical data obtained from vertical gas-solid flow configurations. It is important to note that the fluidization conditions and particle dynamics differ significantly across the various studies. Additionally, the correlations provided correspond to dilute solids flow systems, where volumetric solids concentrations are typically below $<10^{-2}$ kg/m^3. However, while existing studies underscores the importance of frictional losses in solids suspension flow, research on solids friction in dense fluidized beds remains limited.

Regarding the characterization of dense fluidized beds, various methods for assessing the rheological properties have been explored. Table 2 provides an overview of the literature on experimental studies of the rheological characteristics of solids fluidized under dense conditions, specifying the viscometer types employed and the operational conditions explored. Each work investigates different rheological parameters, such as wall shear stress 'τ_w', wall shear rate '$\dot{\gamma}_w$', and effective viscosity 'η'. Fluids exhibit varying responses to an increase in shear rate: the effective viscosity either remains constant (Newtonian fluid) or changes (non-Newtonian fluid). For the latter, as the shear rate increases the effective viscosity can decrease (shear-thinning fluid) or increase (shear-thickening fluid). Moreover, some fluids (e.g., Bingham plastics or pseudoplastic fluids) exhibit a stress threshold at a zero-shear rate (known as the yield stress), beyond which they begin to flow. An understanding of these rheological descriptions is used then in the tailoring of equipment design for each type of suspension and is also crucial for predicting how the flow will vary under different loads (i.e. different levels of solids throughflow). For instance, shear-thickening fluids might require more robust-agitation to move, while shear-thinning fluids flow more easily.

The falling sphere viscometer determines the viscosity of the fluidized bed by measuring the velocity or fall time of a sphere driven by gravity or buoyancy. This velocity can be inferred from the falling/rising time, or by tracking the sphere's motion (Chhabra and Richardson, 2008; Coussot, 2005). Köhler et al. (2021) used this principle to explore the rheological characteristics of a gas-solids emulsion under minimum

Table 1
Summary of the solids-wall friction factor correlations from various literature studies.

Reference	Solids-wall friction factor correlation	Geometric configuration	Properties of the bed solids used
(Jones et al., 1967)	$f = 1.89 \times 10^{-6} \frac{A_0}{\left(\frac{6}{d_p A_0}\right)^{1/2}}$ where 'A_0' is the surface area of the solid particles.	Diameter: 0.03 m Height: 0.54 m	Fused alumina, glass beads, steel, zircon silica d_p: 156–765 µm ρ_S: 2460–7600 kg/m^3
(Konno and Saito, 1969)	$f = 0.0285 \frac{\sqrt{gD}}{u_S}$	Diameters: 0.027 m, 0.047 m Height: 8 m	Copper spheres, glass beads d_p: 120–1050 µm ρ_S: 2500–8900 kg/m^3
(Capes and Nakamura, 1973)	$f = \frac{0.048}{{u_S}^{1.22}}$	Diameter: 0.076 m Height: 4.87 m	Glass beads, steel spheres d_p: 256–2900 µm ρ_S: 2470–7850 kg/m^3 ε_S: 0.03 [−]
(Kmieć et al., 1978)	$f = \frac{0.074}{{u_S}^{0.75}}$	Diameter: 0.04 m Height: 2 m	Silica gel, turnip seed d_p: 683–2240 µm ρ_S: 802–1154 kg/m^3
(Hariu and Molstad, 1949; Özbelge, 1984)	$f = 0.0054 \left(\frac{W_r \rho_g}{\rho_S}\right)^{-0.115} \left[\frac{u_g}{u_r} \cdot \frac{d_p}{D}\right]^{0.339}$ where 'W_r' is the solids loading ratio.	Diameter: 0.0068 m, 0.0135 m	Cracking catalyst, sand d_p: 110–503 µm ρ_S: 980–2710 kg/m^3 ε_S: 0.001–0.02 [−]
(Breault and Mathur, 1989)	$f = 12.2 \frac{(1-\varepsilon)}{\varepsilon^3 u_S}$	Diameter: 0.038 m Height: 2.3 m	Gypsum, limestone, sand d_p: 296–452 µm ρ_S: 2100–2950 kg/m^3
(Garić et al., 1995)	$f = 0.0017 \frac{(1-\varepsilon) u_t}{\varepsilon^3 u_g} \left[\frac{(1-\varepsilon) u_t}{(u_g - u_S)}\right]^{-1.5}$	Diameter: 0.03 m Height:4.4 m	Glass beads d_p: 1200–2980 µm ρ_S: 2507–2641 kg/m^3 ε_S: 0.008–0.085 [−]
(Rautiainen and Sarkomaa, 1998)	$f = f_\infty - \frac{1}{u_S}$ where 'f_∞' is the constant solids friction factor at high solids velocity.	Diameter: 0.192 m Height: 16.2 m	Glass beads d_p: 64–310 µm ρ_S: 2450 kg/m^3 $\varepsilon_S < 0.01$ [−]
(Lech, 2001)	$f = 0.0108 + 0.066 \frac{M_S}{u_S A \rho_S}$	Diameter: 0.05 m Height: 0.953 m	Polyethylene cube, PVC powder, sand d_p: 80–3000 µm ρ_S: 958–2650 kg/m^3 ε_S: 0.03–0.21 [−]
(Jones and Williams, 2003)	$f = \frac{83}{\frac{{M_S}^{0.9}}{M_f} Fr_i^2}$ where 'Fr_i' is the Froude number at the inlet.	Diameter: 0.053 m Height: 50 m	Copper ore, iron powder, PFA d_p: 42–64 µm ρ_S: 2446–5710 kg/m^3
(Mabrouk et al., 2008)	For smooth wall surface: $f^s = 0.022 u_S^{-1.0}$ For rough wall surface: $f^r = 0.051 u_S^{-1.0}$	Diameter: 0.052 m Height: 1 m	Alumina, sand d_p: 170–250 µm ρ_S: 2500–3400 kg/m^3 ε_S: 0.01–0.035 [−]

Table 2
Literature overview of viscometry techniques utilized to study dense gas-solids suspensions.

Method	Bed properties	Rheological properties	Fluid analogy	Reference
Falling sphere	Spherical glass beads d_S: 212–250 μm ρ_S: 2600 kg/m^3 ε_S: 0.61 [−] Condition: u_{mf}	τ_w: 25–150 Pa $\dot{\gamma}_w$: 0–50 s^{-1}	Shear-thinning	(Köhler et al., 2021)
Capillary	Silica sand d_S: 425–710 μm ρ_S: 2600 kg/m^3 ε_S: 0.42–0.46 [−] Condition: u_{mf}	$\dot{\gamma}_w$: 0.2–600 s^{-1} $\eta(\dot{\gamma}_w)$: 10^0–950 Pas	Shear-thinning	(Bakhtiyarov et al., 1996; Bouillard et al., 2014)
		$\dot{\gamma}_w$: 650–2800 s^{-1} $\eta(\dot{\gamma}_w)$: 10^{-3}–10^{-2} Pa s	Shear-thickening	
Rotational	Glass beads d_S: 500–1000 μm ρ_S: 2700 kg/m^3 ε_S: 0.57–0.62 [−] Condition: u_{mf}	$\dot{\gamma}_w$: 10^{-2}–450 s^{-1} $\eta(\dot{\gamma}_w)$: 10^0–600 Pa s	Newtonian, shear-thinning, and shear-thickening	(Bouillard et al., 2014)
	Carbon black powder d_S: 25–330 nm ρ_S: 1830–2350 kg/m^3 ε_S: 0.06–0.42 [−] Condition: u_{mf}	τ_w: 30–850 Pa $\dot{\gamma}_w$: 10–600 s^{-1}	Shear-thinning, and shear-thickening	
	Glass beads ρ_S: 2600 kg/m^3 d_S: 400–1000 μm Condition: u_{mf}	τ_w: 3.5–17 Pa $\dot{\gamma}_w$: 0.08–1.7 s^{-1}	Bingham plastic	(Anjaneyulu and Khakhar, 1995)
	Glass beads d_S: 75 μm ρ_S: 2450 kg/m^3 ε_S: 0.43–0.60 [−] Condition: $0<u_0/u_{mf}<3.8$	$\dot{\gamma}_w$: 10^{-2}–65 s^{-1} $\eta(\dot{\gamma}_w)$: 10^{-1}–5420 Pa s	Newtonian, Bingham plastic, shear-thinning, and shear-thickening	(Kottlan et al., 2018)
Couette	Glass beads ρ_S: 2600 kg/m^3 d_S: 50–210 μm Condition: $0<u_0/u_{mf}<1$	τ_w: 100–290 Pa $\dot{\gamma}_w$: 2.5–20 s^{-1}	Shear-thinning	(Yahia et al., 2020)
	Silica sand d_S: 26 μm ρ_S: 460 kg/m^3 ε_S: 0.43–0.55 [−] Condition: u_{mf}	$\dot{\gamma}_w$: 0.05–0.80 s^{-1} $\eta(\dot{\gamma}_w)$: 1.5–10 Pa s	Pseudoplastic	(Colafigli et al., 2009)

fluidization conditions, with the focus on the drag experienced by the immersed sphere. Their research, which employed magnetic particle tracking, revealed shear-thinning behavior of the fluidized solids and the presence of a yield stress (causing stagnation of the immersed spheres, despite the presence of a net buoyancy force). A subsequent study (Guío-Pérez et al., 2023) conducted using the same methodology, revealed that larger bulk solids increase the effective viscosity perceived by the sphere. This increased viscosity is due to the greater resistance to sphere motion, as there is comparatively less space for the migration of bed solids within the emulsion. It was also noted that non-spherical solids, as compared to spherical ones, increase effective viscosity because of their poorer flowability (they flow and rearrange less easily), thereby offering more resistance. Furthermore, Guío-Pérez et al. (2023) found that an increase in solids density increases the effective viscosity of the suspension by providing greater resistance due to higher inertia. This research highlighted the non-Newtonian nature of gas-solids suspensions at minimum fluidization conditions, as evidenced by a significant yield stress and shear rate-dependent drag on the spheres.

The capillary (Ostwald) viscometer quantifies kinematic viscosity by measuring the amount of time required for a fluid to traverse through a capillary tube (Coussot, 2005; Chhabra and Richardson, 2008). Based on this principle, Bakhtiyarov et al. (1996) studied the effective viscosity of fluidized foundry sand, observing that while the viscosity was not influenced by the overall pressure drop in the capillary tube, it was significantly affected by the tube's length-to-diameter ratio. This effect is primarily attributed to the energy losses in the tube's entrance region.

The rotational viscometer allows the calculation of fluid viscosity from the torque required to rotate a spindle, which induces a shear stress (Chhabra and Richardson, 2008; Bhattad, 2023). In a similar approach, Bouillard et al. (2014) used a four-bladed vane rheometer to examine the rheological properties of powders and nanopowders under fluidized conditions. The results showed that an increase in the shear rate resulted in a transition of the gas-solids behavior from Newtonian to shear-thinning and, eventually, to shear-thickening.

The Couette viscometer quantifies fluid viscosity by measuring the torque between concentric cylinders, thereby gauging the shear stress in the confined fluid (Coussot, 2005; Chhabra and Richardson, 2008). Anjaneyulu and Khakhar (1995) used this principle to study a gas-fluidized bed of glass beads and found the fluidized bed to behave as a Bingham plastic, displaying a constant plastic viscosity above the minimum fluidization level and a reduced yield stress with increased flowrate. Yahia et al. (2020) conducted experiments with an aerated bed Couette rheometer, identifying a Coulomb flow behavior for the granular materials studied. Colafigli et al. (2009) explored the rheological behaviors of fluidized beds using a Couette fluidized-bed rheometer under various bed expansion conditions and shear rates. Their experiments, which focused on homogeneously gas-fluidized fine powders, revealed pseudo-plastic behavior. Kottlan et al. (2018) utilized a Couette viscometer and a setup that entailed an orbiting sphere submerged in a fluid (akin to a rotational viscometer) to study the rheological properties of fluidized powders. They noted that the fluidized solids exhibited shear-thinning, Newtonian, and shear-thickening behaviors, depending on the fluidization velocity and the powder's physical characteristics.

Despite extensive research, a clear understanding of how rheological behaviors influence frictional losses in a bubbling bed subjected to horizontal forced convection remains limited, highlighting the need for further investigation in this area. In summary, the previous literature (see Table 2) lists evidence of varying fluid behaviors, with most studies

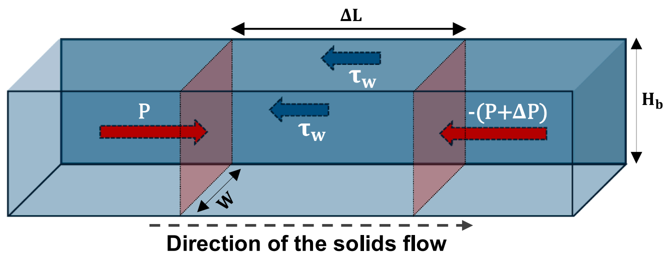

Fig. 1. Schematic illustrating the balance of horizontal forces on a fluidized bed with horizontal solids flow in an open rectangular channel.

identifying non-Newtonian characteristics of bed solids under fluidized and aerated conditions. Given that dense beds, like diluted beds, are expected to exhibit frictional interactions with the wall, their behavior is intricate. Dense beds also exhibit significant viscous forces and strong non-Newtonian behavior. This complexity necessitates adopting a framework that accounts for these effects when predicting the extent of frictional losses, as this could significantly impact the operation's energy expenditure.

The aim of this work is to elucidate the frictional losses in a horizontal flow of solids fluidized under bubbling conditions. The specific objectives are to evaluate the rheological characteristics of the horizontal solids flow, examine the impact of key operational and geometric parameters—such as channel width, bed height, and solids flow velocity—on the frictional parameters, and assess whether existing models for non-Newtonian single-phase flow in channels can describe the frictional behavior of gas-solid flows, proposing a new expression if required. Further, this investigation integrates experimental methods with analytical models from the literature to achieve this. To facilitate the application of advanced measurement techniques and to generate data with quantitative relevance for large-scale industrial processes, the experiments were conducted in a fluid-dynamically down-scaled unit operated under ambient conditions. The use of magnetic solids tracing technique enabled precise quantification of the horizontal solids flowrate, while in-bed pressure probes provided data on friction losses in the flow (horizontal) direction. The scope of the present study is restricted to Geldart B solids fluidized under bubbling conditions.

2. Theory

This section compiles some of the theoretical models used in the description of the flow of generic (non-Newtonian) fluids in rectangular channels. In Section 2.1 the basic expressions related to flow friction in non-circular conduits are presented. Section 0presents three literature power-law models for characterizing the rheology of non-Newtonian flows (such as gas-fluidized solids in general) and which are used in this study. This section provides the framework for calculating key rheological parameters, such as the flow behavior index, flow consistency index, wall shear stress, and wall shear rate. The resulting wall shear stress versus apparent shear rate profiles will be evaluated against experimental data to identify the model that most accurately captures the observed flow behavior. Lastly, Section 2.3 presents the $\mu(I)$ constitutive law, which facilitates understanding of the flow in terms of the granular flow regime.

2.1. Friction in non-circular conduits

While the gas-solids friction dominates the pressure loss in vertical solids transport systems (e.g., risers and downers), in dense fluidized beds that feature a macroscopic horizontal solids transport, the pressure drop along the horizontal direction is primarily governed by solids-solids (particle collisions and friction) and solids-wall interactions (dependent partially upon wall material properties, such as roughness) (Jones et al., 1967; Konno and Saito, 1969; Capes and Nakamura, 1973; Kmieć et al., 1978; Özbelge, 1984; Hariu and Molstad, 1949; Breault and Mathur, 1989; Garić et al., 1995; Rautiainen and Sarkomaa, 1998; Lech, 2001; Jones and Williams, 2003; Mabrouk et al., 2008). The established solids flow pattern, and the corresponding horizontal pressure differences, reflect the varying intensities of these interactions. As solids move horizontally, their collisions and friction with each other and the wall create resistance, which affects the pressure distribution in the bed.

Fig. 1 presents a schematic of the horizontal force balance over a vertical bed slice with a horizontal solids flow in analogy with an open channel flow that is characterized by length ΔL in the flow direction, width W, and fluidized bed height H_b. The horizontal forces include the pressure forces P applied to the front and back faces, and the wall shear stress τ_w exerted along the contact surface with the channel walls.

Under steady state, the difference in pressure along the flow direction can be expressed in relation to the friction force between the solids flow and the walls:

$$P\,A_{cs} - (P + \Delta P)A_{cs} = \tau_w \cdot Per \cdot \Delta L \tag{1}$$

where the flow cross-section is $A_{cs} = W \cdot H_b$, and the wetted perimeter is $Per = W + 2H_b$. These geometric parameters are connected by the concept of the hydraulic diameter:

$$D_h = 4\frac{A_{cs}}{Per} \tag{2}$$

The calculation of the hydraulic diameter for open channel flow has been discussed in the literature (see Chow, 1959 and references therein). Strictly considering the wetted perimeter yields $D_h = 4\frac{WH_b}{W+2H_b}$.

Inserting the generic concept of hydraulic diameter into Eq. (1) yields the following expression for the wall shear stress:

$$\tau_w = \frac{D_h}{4}\frac{\Delta P}{\Delta L} \tag{3}$$

The ratio of the wall shear stress to the inertial force of the fluid flow is calculated using the Fanning friction factor, f_F (Bird et al., 2007), which relates to the Darcy–Weisbach friction factor $f_F = f_D/4$. For a horizontal flow of fluidized solids with a horizontal velocity (u_S) and bed density (ρ_f), as schematized in Fig. 1, it is expressed as follows:

$$f_F = \frac{\tau_w}{\frac{\rho_f {u_S}^2}{2}} \tag{4}$$

The expression can be simplified when an analytical solution to the wall shear stress is available, such as for Newtonian flows in circular cross-sections. Using the analytical solution of the radial profile of the fluid velocity (Hagen–Poiseuille equation) eventually yields $\tau_w = 4\eta u/R$, such that:

$$f_F = \frac{16}{Re} \tag{5}$$

However, lacking a suitable analytic derivation of the wall shear stress for a non-Newtonian flow in an open rectangular channel, such as the one studied here, an alternative approach is needed.

Combining Eqs. (3) and (4) yields the Darcy–Weisbach equation, which provides a framework for relating the pressure drop along the flow direction in a conduit to the cross-sectional geometry, flow velocity, and properties:

$$\frac{\Delta P}{\Delta L} = \frac{2 f_F \rho_f {u_S}^2}{D_h} \tag{6}$$

This expression assumes that the flow is incompressible, steady-state, and characterized by fully developed single-phase conditions (see Appendix A for details). In fluidized solids suspensions, the density exhibits considerable fluctuations at small spatial and temporal scales, primarily due to the bubble flow dynamics. However, in the macroscopic perspective, these local variations aggregate into an overall behavior that generally conforms to that of an incompressible fluid. This implies that, under standard operating conditions, the bed density remains relatively constant despite pressure changes and exhibits a marked degree of homogeneity across a bubbling fluidized bed. Despite the fact that the Darcy–Weisbach equation originates from single-phase flow, its application extends to fluidized beds by considering the bed as a homogenous mixture of the gas and particulate phase. In this approach, the corresponding fluid density is calculated as:

$$\rho_f = (1-\varepsilon_g)\rho_S + \varepsilon_g\rho_g \tag{7}$$

where 'ε_g' is the bed voidage (see measurement details in Farha et al. (2023)).

2.2. Rheological models

Drawing from the analysis in Table 2, which reviews various aerated solids, many studies in the literature adopt the assumption that gas-solids systems can be described as a single-phase flow, treating this mixture as a fluid with specific rheological behavior. This simplification enables the use of rheological models, such as the power-law, to describe the overall behavior of the mixture. The power-law model, also known as the Ostwald-de Waele relationship, is a fundamental tool for analyzing the behavior of non-Newtonian fluids (Chhabra et al., 2001; Chhabra, 2007; Chhabra and Richardson, 2008):

$$\tau = k\dot{\gamma}^n \tag{8}$$

This model provides the basic description of the shear stress τ, as a function of the shear rate $\dot{\gamma}$, i.e., as a function of the relative movement rate between adjacent fluid layers (Chhabra and Richardson, 2008). The power law uses two constants: the flow behavior index n, and the flow consistency index k. Depending on the value of the flow behavior index, the rheological behaviors of fluids are classified as: Newtonian ($n = 1$); shear-thinning (pseudoplastic, $n < 1$), where the viscosity decreases with shear rate; and shear-thickening (dilatant, $n > 1$), where the viscosity increases with shear rate (Chhabra et al., 2001; Chhabra, 2007). The power-law model has been shown to be most effective in describing data for the shear-thinning regime (Chhabra and Richardson, 2008). In contrast, the model struggles to describe shear-thickening fluids that typically exhibit discontinuous or abrupt viscosity changes at specific shear rates, the accurate representation of which requires more complex models with additional parameters.

When applied to study the local flow conditions at the wall, the power-law model [Eq. (8)] becomes:

$$\tau_w = k\,\dot{\gamma}_w^n \tag{9}$$

For Newtonian fluids in circular flow cross-sections, the wall shear rate can be analytically derived, as shown in Eq. (10). Although this expression is not directly applicable to non-Newtonian fluids (e.g., fluidized solids, as presented in Table 2) or non-circular flow cross-sections, it is often used in these cases as an approximation under the concept of apparent shear rate:

$$\dot{\gamma}_a = \frac{8u_S}{D_h} \tag{10}$$

The actual wall shear rate in circular flow cross-sections for non-Newtonian fluids can be calculated from the apparent shear rate using the Rabinowitsch–Mooney equation (Rabinowitsch, 1929; Mooney, 1931; Metzner and Reed, 1955), which is $\dot{\gamma}_w = \dot{\gamma}_a(3n + 1/4n)$. The validity of the Rabinowitsch–Mooney equation for non-Newtonian fluids assumes that the fluid does not exhibit time-dependent behaviors such as thixotropy or rheopexy. This equation is applicable when the fluid properties (such as the flow consistency index and flow behavior index) are constant over the range of shear rates considered. Inserting this expression into Eq. (9) provides the following general expression for non-Newtonian flow in circular cross-sections:

$$\tau_w = k^*\,\dot{\gamma}_a^{n^*} \tag{11}$$

where the two flow indexes correspond to $k^* = (3n + 1/4n)^n$ and $n^* = n$.

Combining the above expressions, the apparent viscosity of a non-Newtonian fluid in circular cross-sections can be evaluated at the wall:

$$\eta = \frac{\tau_w}{\dot{\gamma}_w} = k\left(\frac{3n+1}{4n}\right)^n\left(\frac{8u_S}{D_h}\right)^{n-1} \tag{12}$$

Substituting the above expression yields the Metzner–Reed equation, which defines the Reynolds number for non-Newtonian fluids in circular cross-sections (Metzner and Reed, 1955):

$$Re^* = \frac{\rho_f u_S D_h}{\eta} = \frac{\rho_f {u_S}^{2-n}\,D_h^n}{8^{n-1}\,k\left(\frac{3n+1}{4n}\right)^n} \tag{13}$$

Consideration of non-Newtonian flow in non-circular cross sections entails a higher level of complexity. This study examines three models from the literature that extend the above expressions for non-Newtonian flow, derived from the power-law model [Eq. (9)] and the Rabinowitsch–Mooney equation [Eq. (13)], by comparing them against measurements from this work. Note that these models are applied to more complex geometries, including open channels.

Kozicki et al. (1966) developed a model for application to open channels with cross-sections of arbitrary geometry. For rectangular open channels, they derived a Reynolds number, Re^*_{KT}, based on a two-shape-factor framework (Kozicki et al., 1966; Kozicki and Tiu, 1967):

$$Re^*_{KT} = \frac{\rho_f u_S^{2-n} D_h^n}{8^{n-1} K_{KT}\left[\frac{a+bn}{n}\right]^n} \tag{14}$$

where a and b are geometry-dependent constants whose analytical solutions have been further developed by Kozicki and Tiu (1967), Tiu et al. (1968), Kozicki and Tiu (1971), building upon the foundational work of Straub et al. (1958):

$$a = \frac{1}{2}\left(\frac{\lambda}{1+\lambda}\right)^2\left[1 - \frac{32}{\pi^3}\sum_0^\infty \frac{(-1)^{n^*}}{(2n^*+1)^3}\,\frac{1}{cosh\frac{(2n^*+1)}{2}\pi\lambda}\right]^{-1} \tag{15}$$

$$b = a[3\phi - 1] \tag{16}$$

where

$$\phi = \frac{1 - \frac{32}{\pi^3}\sum_0^\infty \frac{(-1)^{n^*}}{(2n^*+1)^3}\,\frac{1}{cosh\frac{(2n^*+1)}{2}\pi\lambda}}{1 - \frac{192}{\pi^5\lambda}\sum_0^\infty \frac{1}{(2n^*+1)^5}\,tanh\frac{(2n^*+1)}{2}\pi\lambda} \tag{17}$$

$$\lambda = \frac{W}{2H_b} \tag{18}$$

The model of Kozicki et al. has been applied in various studies to analyze the behaviors of non-Newtonian fluids in open channels with different cross-sectional shapes (Burger et al., 2010; Burger et al., 2015; Ayas et al., 2019; Ayas et al., 2021).

Furthermore, the Fanning friction factor [Eq. (5)] can be generalized for non-circular cross-sections based on geometric parameters from the Kozicki et al. model, as shown below (Kozicki and Tiu, 1967; Tiu et al., 1968; Kozicki and Tiu, 1971):

$$f_F = \frac{C}{Re^*} \Rightarrow \frac{16(a+b)}{Re^*} \tag{19}$$

Note that for a given geometry, C is a constant for a fully developed flow under laminar conditions (Metzner and Reed, 1955; Kozicki and Tiu, 1967; Chhabra and Richardson, 2008). In circular geometries, $a =$

Table 3
Summary of the rheological parameters for the considered models from the literature.

	Model 1	Model 2	Model 3
References	(Kozicki et al., 1966; Kozicki and Tiu, 1967; Tiu et al., 1968; Kozicki and Tiu, 1971)	(Kostic and Hartnett, 1984; Ayas et al., 2019; Ayas et al., 2021)	(Delplace and Leuliet, 1995)
Reynolds number, Re^* [−]	$\frac{\rho_f u_S^{2-n} D_h^n}{8^{n-1} K_{KT} \left[\frac{a+bn}{n}\right]^n}$	$\frac{\rho_f u_S^{2-n} D_h^n}{8^{n-1} K_{KH} \xi \left[\frac{3n+1}{4n}\right]^n}$	$\frac{\rho_f u_S^{2-n} D_h^n}{\beta^{n-1} K_{DL} \left[\frac{24n+\beta}{(24+\beta)n}\right]^n}$
Flow behavior index, n^* [−]	n	n	n
Flow consistency index, k^* [Pa s^n]	$K_{KT}\left[\frac{a+bn}{n}\right]^n$	$K_{KH}\xi\left[\frac{3n+1}{4n}\right]^n$	$K_{DL}\left[\frac{24n+\beta}{(24+\beta)n}\right]^n$
Wall shear rate, $\dot{\gamma}_w$ [s^{-1}]	$\left[\frac{a+bn}{n}\right]\left[\frac{8u_S}{D_h}\right]$	$\xi^{1/n}\left[\frac{3n+1}{4n}\right]\left[\frac{8u_S}{D_h}\right]$	$\left[\frac{24n+\beta}{(24+\beta)n}\right]\left[\frac{\beta u_S}{D_h}\right]$
Wall shear stress, τ_w [Pa]	$K_{KT}\left[\frac{a+bn}{n}\right]^n\left[\frac{8u_S}{D_h}\right]^n$	$K_{KH}\xi\left[\frac{3n+1}{4n}\right]^n\left[\frac{8u_S}{D_h}\right]^n$	$K_{DL}\left[\frac{24n+\beta}{(24+\beta)n}\right]^n\left[\frac{\beta u_S}{D_h}\right]^n$

1/2 and *b* = *1/2*, yielding the geometric parameter *C* = *16* [Eq. (5)]. However, in non-circular cross-sections, Eq. (19) remains elusive due to non-linear momentum effects caused by the viscosity's dependence upon the rate of shear strain.

The second model considered in this work, as proposed by Kostic and Hartnett (1984), merges the geometrical parameters introduced by Kozicki et al. (1966) with the Metzner–Reed framework (Metzner and Reed, 1955), to yield the following Reynolds number:

$$Re^*_{KH} = \frac{\rho_f u_S^{2-n} D_h^n}{8^{n-1} K_{KH} \xi \left[\frac{3n+1}{4n}\right]^n} \tag{20}$$

where ξ is the extended geometry-flow function:

$$\xi = \left[\frac{4(bn+a)}{3n+1}\right]^n \tag{21}$$

This model has been simplified by Ayas et al. (2019), who primarily focused on shear-thinning fluids in rectangular ducts and proposed a linearization of the geometry-flow function with the flow behavior index:

$$\xi = \left(\frac{C}{16} - 1\right) n + N \tag{22}$$

where *N*=*1* (since ξ tends to unity as the flow index n approaches zero). This method was later empirically validated within the range of $0 < n < 2$ (Ayas et al., 2021).

Lastly, Delplace and Leuliet (1995) contributed an additional model by addressing the fact that while the geometric coefficients (*a*, *b*) accommodate the characteristics of non-circular cross-sections, the factor 8^{n-1} [denominator in Eqs. (14) and (20)] pertains exclusively to circular cross-sections. Consequently, they proposed the following expression for the Reynolds number:

$$Re^*_{DL} = \frac{\rho_f u_S^{2-n} D_h^n}{\beta^{n-1} K_{DL} \left[\frac{24n+\beta}{(24+\beta)n}\right]^n} \tag{23}$$

where $\beta = C/2$.

Table 3 summarizes the three literature models considered in this study, selected from the limited literature on non-Newtonian flows in non-circular cross-sections. These models will be evaluated below to determine their applicability in characterizing fluidized solids flow, as they were originally developed for non-Newtonian single-phase flows.

2.3. *Granular flow rheology*

In granular systems, the macroscopic friction coefficient is defined as the ratio of the wall shear stress to the normal stress exerted by the particles on the wall (MiDi, 2004; Jop et al., 2006):

$$\mu = \frac{\tau_w}{P_p} \tag{24}$$

where the particle pressure, P_p, can be determined experimentally (see for example Campbell and Wang, 1990) or from correlations with fluid-dynamical parameters such as the bubble size (see for example Campbell and Wang, 1991).

In addition to the friction coefficient, the inertial number I, characterizes the flow by comparing two timescales: the time governing particle inertia (indicative of the ability of particles to rearrange) t_P, and the deformation time of the granular material when under a given shear $t_{\dot{\gamma}_w}$ (MiDi, 2004; Jop et al., 2006):

$$I = \frac{t_P}{t_{\dot{\gamma}_w}} = \frac{\sqrt{\rho_S d_S^2 / P_p}}{1/\dot{\gamma}_w} \tag{25}$$

A notable advancement in the understanding of granular flows has

Table 4
Main parameters used in the fluid-dynamical scaling.

Parameter	Units	Hot unit	Cold flow model
Temperature	°C	900	24
Fluidization gas	–	Hot air or flue gas	Air
Gas density (ρ_g)	kg/m^3	0.359	1.187
Gas viscosity (μ_F)	m^2/s	1.4×10^{-4}	1.54×10^{-5}
Bed geometry	m	L_{HOT}	0.12 L_{HOT}
Bed material	–	Silica sand	Bronze
Particle density (ρ_S)	kg/m^3	2650	8770
Mean particle diameter (d_S)	μm	950	125
Gas superficial velocity (u_0)	m/s	$u_{0,HOT}$	$\sqrt{0.12}\ u_{0,HOT}$
Minimum fluidization velocity (u_{mf})	m/s	0.31	0.108
Solids mean horizontal velocity (u_S)	m/s	$u_{S,HOT}$	$\sqrt{0.12}\ u_{S,HOT}$
Solids lateral dispersion coefficient (D_S)	m^2/s	$D_{S,HOT}$	0.042 $D_{S,HOT}$

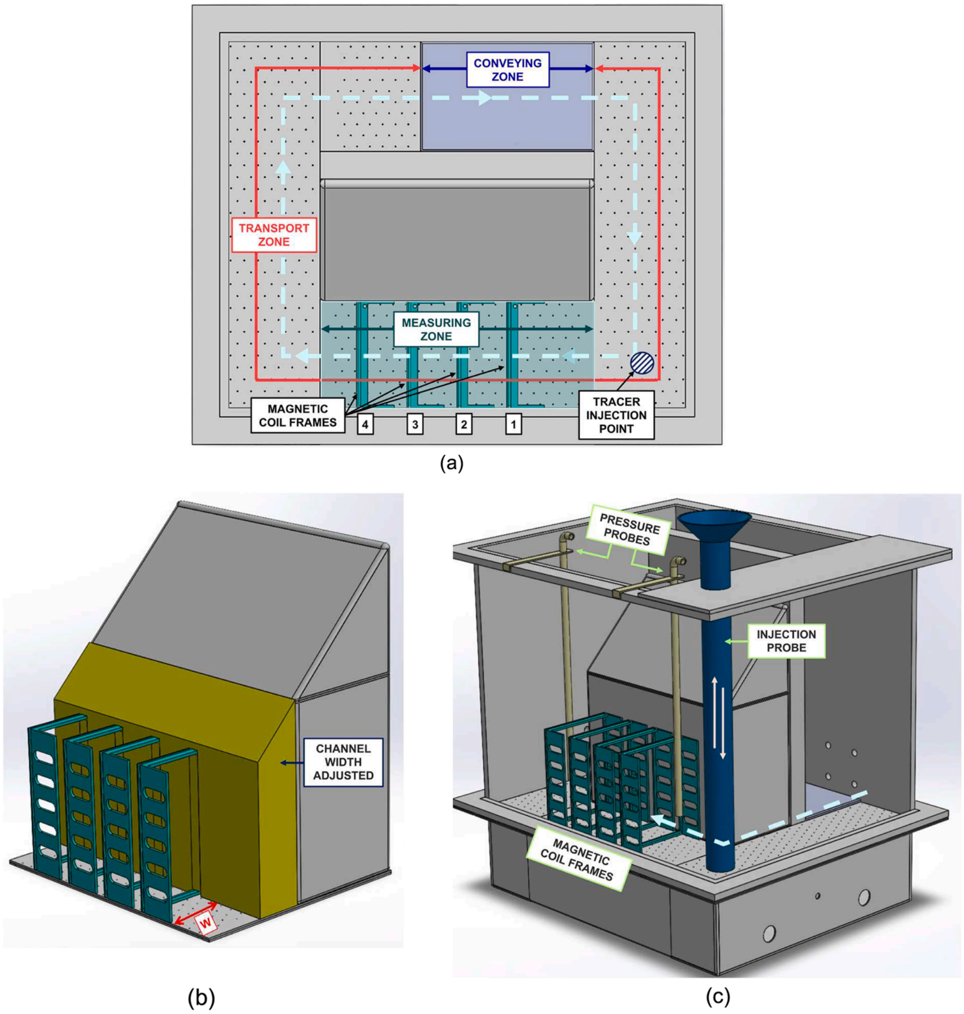

Fig. 2. Fluid-dynamically down-scaled model used for the experiments. (a) Top view, indicating the direction of the forced horizontal solids circulation, and the locations that delineate the conveying, transport, and measuring zones. (b) Lateral view, showcasing how the channel width is adjusted by insertion of a rigid module. (c) (c) Lateral view, indicating the injection probe, pressure probes, and magnetic coil frames.

been the development of the constitutive law (Jop et al., 2006) that links the macroscopic friction coefficient, μ, to the inertial number, I, thereby providing a framework for predicting the flow behavior of dense granular materials. The $\mu(I)$ constitutive law establishes a correlation between the above two dimensionless numbers through (MiDi, 2004; Jop et al., 2006):

$$\mu(I) = \mu_S + \frac{\mu_2 - \mu_S}{I_0/I + 1} \qquad (26)$$

where μ_S is the static friction coefficient (at low inertial numbers), μ_2 represents the friction coefficient at high inertial numbers, and I_0 is a constant that represents the rate of transition between the two states as the inertial number I increases.

The constitutive law relation [Eq. (26)] describes the behavior of a granular flow as it transitions from a quasi-static regime, through a dense flow regime to eventually, a collisional regime (da Cruz et al., 2005; Chevoir et al., 2009). In the quasi-static regime, the material exhibits minimal frictional variation, behaving similar to a solid due to the dominant inter-particle contacts and the substantial influence of a confining pressure that restricts particle movement. At higher values of the inertial number, the flow enters the intermediate dense flow regime, in which the material maintains a liquid-like state that is marked by an increased interplay of particle sliding and collisions, leading to a higher friction coefficient. Finally, with a significant increase in the inertial number, the collisional or rapid flow regime is attained, wherein inertial effects predominate, and the friction coefficient either reaches a plateau or diminishes as particle collisions take precedence, with the confining pressure exerting weaker control over the flow behavior.

3. Methodology

3.1. Experimental work

3.1.1. Experimental setup

This work implements a fluid-dynamical down-scaling methodology to design experiments that resemble a large-scale hot flow of solids, conducted under ambient conditions. The use of ambient conditions

Table 5
Experimental matrix.

Parameter	Units	Downscaled	Upscaled
Fixed bed height (H)	m	0.08–0.10	0.67–0.83
Channel width (W)	m	0.07–0.12	0.58–1.00
Conveyed solids velocity (u_S)	m/s	0–0.035	0–0.101

increases operational flexibility and the possibilities to implement advanced measurement techniques, while still delivering results that are relevant for industrial energy conversion applications. The experimental unit is designed and operated according to Glicksman's simplified set of scaling laws (Glicksman et al., 1993), ensuring dynamic similarity by preserving key dimensionless groups that govern the conservation of momentum in gas-solid systems:

$$\frac{u_0^2}{gD}, \frac{\rho_S}{\rho_g}, \frac{u_0}{u_{mf}}, \frac{G_S}{\rho_S u_0}, \frac{L_1}{L_2}, \varphi, \text{ PSD}$$

Adhering to these dimensionless parameters allows the scaling approach to accurately replicate, under ambient lab-scale conditions, the fluid dynamics of a hot, large-scale system (8.3× length-scaling, 900 °C in this work). This scaling method has been extensively validated—see Djerf et al. (2021) for large-scale (300 MW) validation in the literature.

In line with the scaling, spherical bronze particles (particle diameter 125 μm; particle density 8770 kg/m^3) are used as bed material to simulate the behaviors of sand (725 μm, 2650 kg/m^3) under hot conditions.

Table 4 summarizes key parameters of both the cold flow model and the represented hot unit; further details of the scaling parameters are provided in Farha et al. (2023).

The bed material in this study falls under Geldart B-type classification, characterized by the onset of bubbling at or just above the minimum fluidization velocity. As bubbles rise, they grow through coalescence, with minimal gas back-mixing in the dense phase (Geldart, 1973; Kunii and Levenspiel, 1991).

The fluid-dynamically down-scaled unit employed (Fig. 2) has a footprint of 0.5 m × 0.4 m and a height of 0.5 m. A rigid central block creates the annular region that entails the solids circulation loop. The annular region consists of two differentiated zones: the conveying zone, where convection of the horizontal solids flow is forced by means of air injection (Fig. 2a, see Farha et al. (2023) for details), and the transport zone, where the solids move horizontally while being fluidized under bubbling conditions. The flow of the fluidization agent to the conveying and transport zones is independently regulated via mass flow controllers, ensuring a stable airflow. A fluidization number (u_0 /u_{mf}) of 3 is maintained in the transport zone throughout all experiments, ensuring bubbling fluidization for the Geldart B-type solids used in this study. Pressure transducers placed around the experimental rig enable real-time monitoring of solids density and circulation rate, allowing precise control of bubbling conditions in the transport zone.

A section of the transport zone, referred to as the measuring zone (length of 0.23 m), was selected to carry out solids velocity and pressure drop measurements. The standard width of the measuring zone is 0.12 m, but it can be reduced by adding an extension to the central block (see Fig. 2b). The bed height can be varied by changing the amount of bed material in the system.

Within the measurement zone, four magnetic solids tracing (MST) coil frames are installed to measure the lateral solids velocity (see Section 3.1.3 In addition, in-bed pressure probes are installed at both ends of the measurement section (see Fig. 2c) to allow measurements of the bed density and horizontal pressure drop along the measuring zone.

Table 6
Properties of the bed and tracer solids used in the present work.

Parameter	Units	Bed solids	Tracer solids
Material	–	Bronze	Iron-based alloy
Particle density (ρ_S)	kg/m^3	8770	7988
Bulk density (ρ_B)	kg/m^3	5522	4520
Particle size distribution d_{10}-d_{50}-d_{90}	μm	80–112–132	25–69–123
Sauter mean diameter (d_{32})	μm	125	102
Ar$^{1/3}$	–	8.386	6.127
Minimum fluidization velocity (u_{mf})	m/s	0.074	0.039
Magnetic susceptibility	–	0	0.9

3.1.2. *Test matrix*

The parametrization of the results incorporates variations in: conveyed solids velocity (0–0.035 m/s, a range attained by varying the air flow injected into the conveying zone, see Fig. 2a); settled bed height (0.08–0.1 m); and channel width (0.07–0.12 m) (for up-scaled values of these operational parameters, see Table 5). The upper limits for the first two parameters are set based on the need to avoid bed material loss through splashing. The lower limit for the bed height is constrained by the design of the conveying section, which is not suitable for forcing a solids flow at lower bed heights. The lower bound of the channel width is defined by geometric constraints: a reduction beyond this limit hampers accurate pressure profile extraction and complicates the placement of the pressure probes. The fluidization velocity in the transport zone is kept constant at 0.225 m/s ($u_0/u_{mf} = 3$). Although fluidization velocity affects bed density and may impact frictional forces, the extent of this effect is outside the scope of the present study. In total, this study encompasses 27 distinct operational cases, each of which is replicated thrice to ensure statistical robustness.

3.1.3. *Measurement techniques*

The solids circulation flow rate was assessed by measuring the bed voidage (proportional to the solids concentration) and the solids mean horizontal velocity. Bed voidage, ε_g, used for calculating bed density [Eq. (7)], is measured with immersed pressure probes, as detailed in (Farha et al., 2023). The determination of the solids velocity u_S, is done using the magnetic solids tracing (MST) technique (Farha et al., 2023). This involves measuring the impedance change generated in magnetic coil frames when ferromagnetic solids tracers, which mimic the bulk solids, move through the coils. The impedance time series can then be converted to transient profiles of the solids concentration at the position of each coil. The solids mean velocity can be evaluated by fitting the experimental concentration transients to a theoretical flow model, which assumes the solids follow convective-dispersive transport. Thus, the transient concentration at a given location can be expressed as Versteeg and Malalasekera (2007):

$$\frac{\partial C_i}{\partial t} = \left(D_S \times \frac{\partial^2 C_i}{\partial x^2}\right) - u_S\frac{\partial C_i}{\partial x} \tag{27}$$

For each experiment, a 200 g batch of tracer solids was introduced 0.14 m upstream of Coil 1 (see injection probe in Fig. 2b), and the transient impedance response at each of the four coils was sampled at 100 Hz for 6 min. The coils are located at the following distances downstream of the solids tracer injection: 0.140, 0.195, 0.250 and 0.305 m. It is important to note that the quantity of tracer injected represents only 0.25–0.32 % of the total solids inventory, thereby ensuring that it does not interfere with the assumption of steady-state conditions. This is corroborated by monitoring the pressure signals, which demonstrate consistency of the pressure measurements before and after injection of the tracer, affirming the stability of the system. The tracer solids are removed from the bed after each experiment. Table 6 lists the physical properties of both the bed solids and the ferromagnetic tracer used in the experiments. Details on the extraction of data pairs [solids velocity, solids dispersion coefficient] from MST experiments are provided in Appendix B.

Furthermore, measurements of the horizontal pressure drop are made via the pressure transducers (Huba Control, piezoelectric type; precision >0.5 % fs; range ±20 mbar) sampled at 5 Hz. The pressure measurement data under steady-state conditions are time-averaged over a 180 s interval for each experimental run for subsequent processing. The probes are positioned at the midpoint of the channel width, at a consistent bed height of 0.525 m from the distributor plate. One probe is located at the beginning of the measurement zone, while the other is placed at the end.

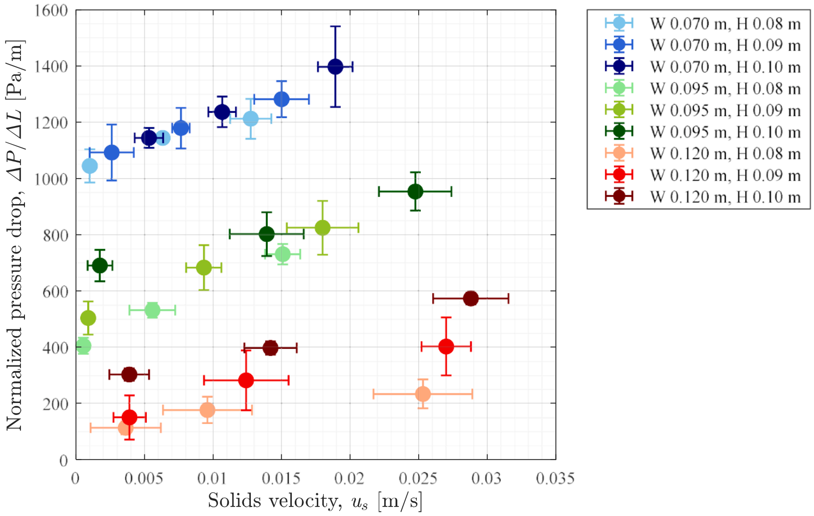

Fig. 3. Normalized pressure drop in the horizontal direction as a function of the horizontal solids velocity.

3.2. Data processing

Three parameters are measured: bed voidage; horizontal pressure gradient; and horizontal solids velocity. From these data, the Fanning friction factor and wall shear stress are calculated using Eqs. (6) and (3), respectively. This study compares three extended models (see Table 3) that apply the power-law framework [Eq. (8)] and the Rabinowitsch–Mooney equation for non-Newtonian flows in non-circular cross-sections. Subsequently, for each of the three models considered, the flow behavior and apparent flow consistency indices are fitted to the measurement-derived wall shear stress values (see last row in Table 3). Thereafter, other parameters, such as the generalized Reynolds number Re^* and the wall shear rate $\dot{\gamma}_w$, can also be calculated (see Table 3).

4. Results and discussion

4.1. Pressure drop variation

Fig. 3 presents the normalized horizontal pressure drop measured (0–1600 Pa/m) against the horizontal mean velocities of the solids (0–0.035 m/s) extracted form MST measurements. The expected general trend of increased pressure drop for higher solids velocities, higher bed height and narrower channel widths is observed. Note that the error bars in the figures (both horizontal and vertical) represent the standard deviation calculated from three independent repetitions of each experimental condition.

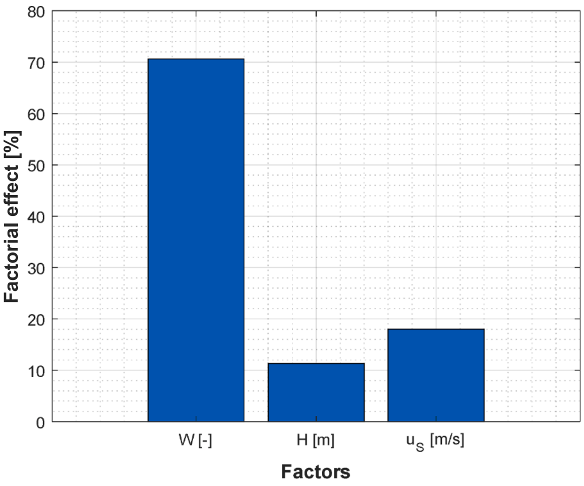

Fig. 4. Evaluation of the influence of operational conditions (channel width 'W', fixed bed height 'H' and solids velocity 'u_S') on the normalized pressure drop attributed to induced solids circulation, in the regression model.

Unlike equivalent measurements in liquids, defining the effective wall perimeter for a channel containing a fluidized bed with horizontal solids movement is not straightforward. The role of the gas distributor plate in defining the hydraulic diameter remains debated in fluidized bed setups (Grace et al., 2006). As shown in Fig. 3, the measurements indicate that a decrease in channel width is associated with an increase in pressure drop, highlighting the dominant role of bed-wall interactions in causing flow resistance. This suggests that shear stress is primarily governed by the effect of the sidewalls, while friction with the bottom (gas distribution) plate is considerably less significant. The friction at the sidewalls intensifies as the channel width decreases due to a steeper normal velocity gradient. Additionally, the diminishing effect of bed height at the narrowest width indicates that the bottom plate has a limited contribution to shear resistance, likely due to a lubrication effect caused by gas injection. Thus, the measurement data support the exclusion of the gas distributor plate from the wetted perimeter calculation, which then simplifies to:

$$D_h = 4\frac{WH_b}{2H_b} = 2W \qquad (28)$$

The influence of incorporating channel width in the wetted perimeter is presented in Appendix E, where an additional result—the wall shear stress–shear rate plot—is provided for comparison.

Regression analysis (yielding $R^2 = 0.964$) indicates that channel width variation confers the most significant factorial effect, contributing 70.61 %, as shown in Fig. 4. Conversely, the fixed bed height and solids velocity contribute to a much lesser extent, at 11.4 % and 18.0 %, respectively, and display a direct dependence with the normalized pressure drop. Fig. 4 further illustrates that bed height has a minor impact on friction compared to the channel width and solids velocity, suggesting that the increase in wetted perimeter (see Eq. (28)) has a negligible effect. The channel width significantly influences the normalized pressure drop, exhibiting an inverse relationship (Fig. 3), likely due to its effect on flow patterns, which is characteristic of non-Newtonian fluids. Additionally, the impact of velocity varies with the cross-sectional area available for flow, indicating a dependence on shear rate and highlighting the non-Newtonian behavior of the fluid.

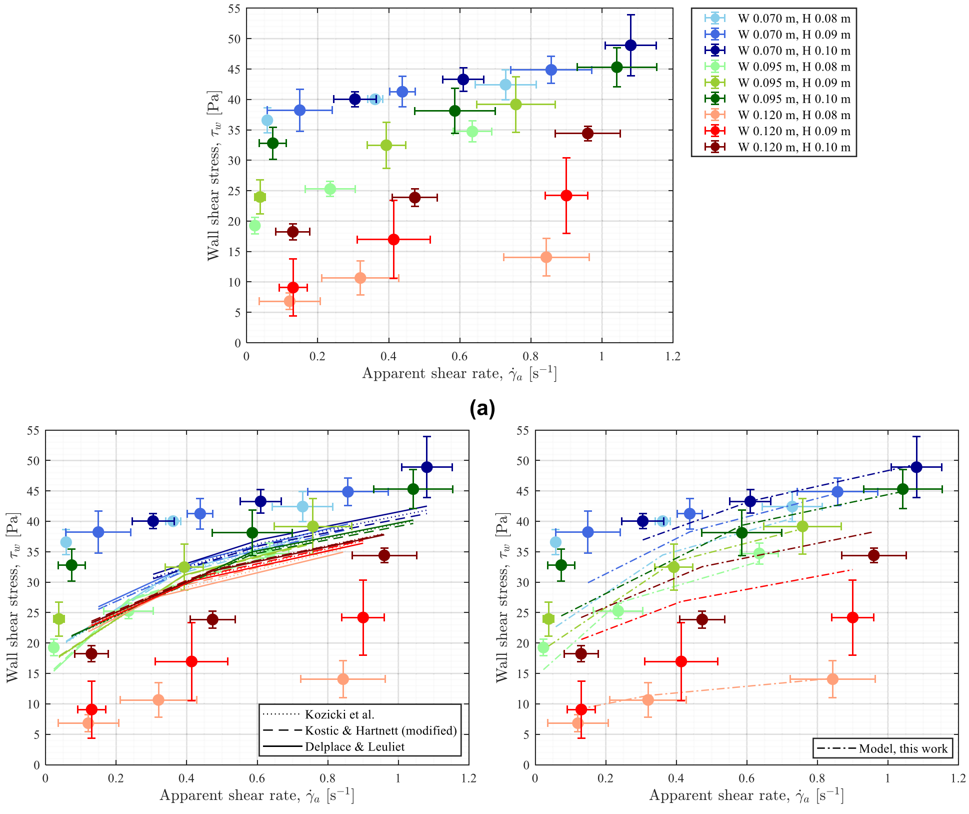

(a)

(b)

(c)

Fig. 5. Wall shear stress as a function of apparent shear rate for various channel widths and bed heights. (a) Experimental data. (b) Comparison of three literature models–see Table 3 –with experimental data. (c) Comparison of the proposed fitted expressions from this work [Eqs. (29) and (30)] with experimental values.

4.2. Rheological characterization

Fig. 5a shows the relationship between the wall shear stress [Eq. (3)] and the apparent shear rate [Eq. (10)], for various combinations of channel width and bed height as obtained from the measurements. The consistently non-linear relationship confirms the non-Newtonian behavior of fluidized solids throughflow. Additionally, the figure shows that, for a given shear rate, the wall shear stress increases with bed height and decreases with channel width. To complete the rheological characterization of this system, it is necessary to consider an expression that accounts for both the non-Newtonian behavior of the fluid and the non-ideal (non-circular) cross-section. The models introduced in Section 2.2 (see Table 3) are applied to the results shown in Fig. 5a.

Table 7 presents the fitted values of the flow consistency index constant (K) and the flow behavior index (n) for each of the three models considered, along with the resulting flow consistency index (k^*) for each of the geometric configurations. It is important to note that conventional rheological models exhibit geometry-dependent variations in k^*, despite being developed for single-phase flows.

The flow behavior index, which is consistent across all models, yields an average value of 0.24 after fitting, indicating that the fluidized gas-solids suspension exhibits shear-thinning behavior ($n < 1$). The flow consistency index constant for the three different models ranges from 34–37 Pa s^n. Although the magnitude of geometric variations in k^* is small (<2.0 %) within each model, the observed qualitative trends are consistent—k^* increases with bed height and decreases with channel width.

Fig. 5b compares the wall shear stress values provided by each of the three rheological models considered (lines) with the experimentally derived values (markers). The comparison reveals significant discrepancies between the modeled and experimental data (R^2 = 0.29–0.35), primarily because the geometric parameters were not included in any of the rheological models considered. Notably, none of the three models considered were originally developed for or previously applied to gas-fluidized solids systems.

Consequently, it becomes of particular interest to develop a model that incorporates the impact of geometry on wall shear stress in fluidized gas-solids systems. Building on the generalized Rabinowitsch–Mooney model (Rabinowitsch, 1929; Mooney, 1931), this study presents an equation for the flow consistency index of the investigated solids in rectangular open-channels, incorporating the channel width and fluidized bed height as geometry parameters:

$$k^* = K[f(W, H_b)]^n \tag{29}$$

where both variables are used in their dimensionless forms and weighted with respective coefficient, C:

$$k^* = K\left[C_W\left[\frac{W}{d_S}\right] + C_{H_b}\left[\frac{H_b}{d_S}\right]\right]^n \tag{30}$$

Fitting to the measurement-derived data from this work yields $C_W = -5.85 \times 10^{-3}$ and $C_{H_b} = 6.51 \times 10^{-3}$.

Table 8 displays the values of the main rheological parameters obtained for the proposed model, featuring a flow behavior index of 0.23 and a flow consistency index of 35.78 Pa s^n. These results do not differ significantly from the outcomes from the three literature models previously considered. However, in contrast to those models, the k^* values reflect a significant impact of the channel's geometry (channel width and bed height).

The results in Table 8 highlight that while the fundamental rheological parameters of the system—K and n^*—remain unchanged, k^* incorporates geometric parameters and therefore varies with channel

Table 7
Fitted values of the main rheological parameters for each of three literature models considered.

Rheological models	Geometric parameters, (W, H) [m]	Flow consistency index, (Geometry dependent) k^* [Pa s^n]	Flow consistency index constant, K [Pa s^n]	Flow behavior index, $n = n^*$ [−]
Model 1 (Kozicki et al., 1966; Kozicki and Tiu, 1967; Tiu et al., 1968; Kozicki and Tiu, 1971)	0.070, 0.08	40.05	$K_{KT} = 34.98$	0.24
	0.070, 0.09	40.60		
	0.070, 0.10	41.05		
	0.095, 0.08	38.43		
	0.095, 0.09	39.09		
	0.095, 0.10	39.64		
	0.120, 0.08	37.00		
	0.120, 0.09	37.75		
	0.120, 0.10	38.37		
Model 2 (Kostic and Hartnett, 1984; Ayas et al., 2019; Ayas et al., 2021)	0.070, 0.08	41.85	$K_{KH} = 36.82$	0.24
	0.070, 0.09	42.04		
	0.070, 0.10	42.19		
	0.095, 0.08	41.32		
	0.095, 0.09	41.53		
	0.095, 0.10	41.72		
	0.120, 0.08	40.85		
	0.120, 0.09	41.09		
	0.120, 0.10	41.30		
Model 3 (Delplace and Leuliet, 1995)	0.070, 0.08	39.61	$K_{DL} = 35.62$	0.24
	0.070, 0.09	40.10		
	0.070, 0.10	40.52		
	0.095, 0.08	38.30		
	0.095, 0.09	38.82		
	0.095, 0.10	39.27		
	0.120, 0.08	37.28		
	0.120, 0.09	37.80		
	0.120, 0.10	38.26		

Table 8
Rheological parameters for the proposed model [Eqs. (29) and (30)].

Geometric parameters, (W, H) [m]	Flow consistency index, (Geometry-dependent) k^* [Pa s^n]	Flow consistency index constant, K [Pa s^n]	Flow behavior index, n^* [−]
0.070, 0.08	43.51	35.78	0.23
0.070, 0.09	46.21		
0.070, 0.10	48.46		
0.095, 0.08	37.07		
0.095, 0.09	41.32		
0.095, 0.10	44.46		
0.120, 0.08	14.57		
0.120, 0.09	32.87		
0.120, 0.10	38.64		

width and bed height. This indicates that geometric confinement effects influence shear stress distribution, despite not altering the intrinsic material properties. Thus, introducing geometry into the shear stress expression provides a means to account for its impact in zero-dimensional descriptions. However, for generic spatially-resolved descriptions, this adjustment is unnecessary, as the mesh inherently captures geometric effects.

Fig. 5c compares the experimentally-derived values of the wall shear stress (markers) to those obtained using the fitted expressions proposed in this work [Eqs. (29) and (30)], (dashed curves in the figure). The model effectively captures the trends for different channel configurations, particularly for channel widths in the range of 0.07–0.095 m, yielding $R^2 = 0.785$. However, it should be noted that the applicability of the model is confined by the operational (Geldart B-type solids, limited ranges for the fluidization number, bed height) and geometric boundaries (channel width, bed height) applied in the present tests and cannot be generalized to other fluidized bed systems.

The higher R^2 value of the proposed model, compared to the considered single-phase flow models available in the literature (see Table 3), stems from highlighting the impact of channel geometry (width and bed height) through the coefficients C_W and C_{H_b}. Unlike single-phase flow, dense gas-solid systems exhibit compressible behavior, non-uniform stress distributions, and local defluidization. These phenomena are especially significant in connection with geometric singularities, leading to stronger sensitivity of flow friction to wall and corner effects.

Fig. 6 compares the rheograms (using the wall shear rate rather than the apparent shear rate) obtained for the experimental cases in this work (red markers) with the data from previous works with aerated/fluidized solids acquired using four different rheometric techniques: falling sphere, capillary, rotational, and Couette. Note that the expression derived in this work (see the equation in Konno and Saito, 1969) appears as a straight line in this log-scale plot due to its formulation being based on the power-law model [Eq. (8)]. The shear stress-strain relationship observed for the set-up used in the present work exhibits shear-thinning behavior, consistent with most equivalent data previously reported in the literature (see Table 2). Despite this, the specific correlation between shear rate and shear stress is strongly case-dependent, highlighting the significant roles of the geometric setup, flow conditions, experimental methods, and the gas-solids pair used. Due to the differences among these factors in various studies, direct comparisons are not straightforward.

The findings presented by Köhler et al. (2021), Bouillard et al. (2014), Kottlan et al. (2018), Bakhtiyarov et al. (1996), and Yahia et al. (2020) demonstrate a shear-thinning trend, mirroring the behavior observed in the present study. Köhler et al. (2021) experimented with glass beads under minimum fluidization conditions using the falling sphere viscometry technique. Since the researchers experimented with spheres of different sizes/densities to achieve various shear rates, the results are challenging to compare directly due to the nature of the technique. Bouillard et al. (2014) used rotational viscometry to study glass beads and carbon black powder under minimum fluidization condition. The finer carbon black particles (25–330 nm) exhibited lower stress-strain trend, whereas their experiments with coarser glass beads (500–1000 μm) showed higher trend compared to the present study. Kottlan et al. (2018) observed a variety of rheological behaviors using rotational viscometric technique for glass beads—including Newtonian, Bingham plastic, shear-thinning, and shear-thickening—across different aeration velocities. They noted a decrease in wall shear stress at higher aeration levels due to reduced frictional forces. The present study's

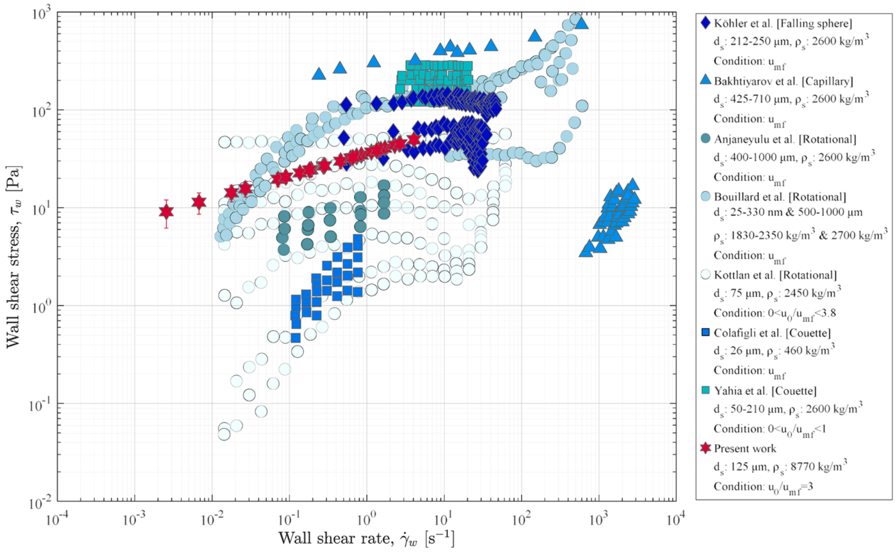

Fig. 6. Rheograms of the data from the present work compared to literature data (referenced in Table 2).

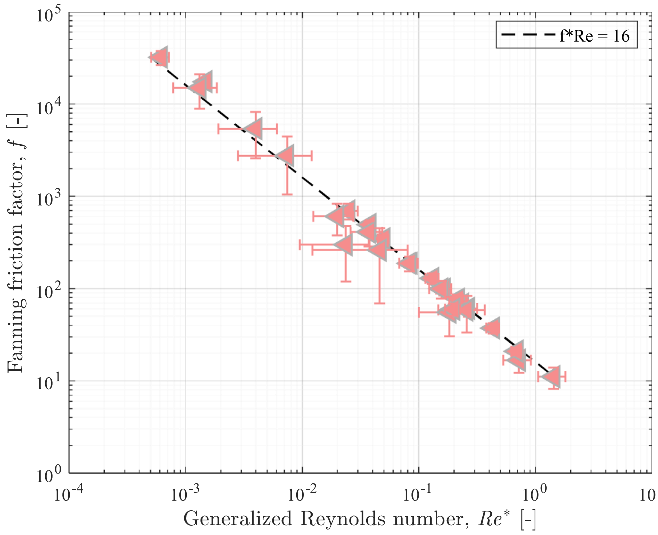

Fig. 7. Fanning friction factor as a function of the generalized Reynolds number.

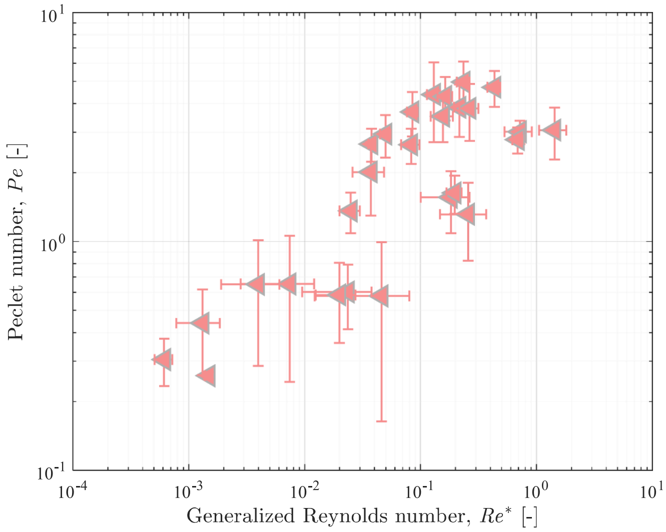

Fig. 8. Péclet number versus generalized Reynolds number.

results align closely with the work of Kottlan et al. (2018) at lower aeration rates, but the particle density here is about three times higher. Bakhtiyarov et al. (1996), using a capillary viscometer, detected shear-thinning behaviors for fluidized sand particles at shear rates in the range of 0.2–600 s^{-1} and shear-thickening behaviors at shear rates in the range of 650–2800 s^{-1}. In the shear-thinning range, the stress-strain trend was higher than in the present study, primarily due to larger particle sizes (425–710 μm) used. The findings of Yahia et al. (2020) using Couette viscometry reported higher wall shear stresses, constrained to a fluidization number of 0.4. Note that higher stress-strain trends are often seen below minimum fluidization due to insufficient fluidization reducing inter-particle friction. Lastly, in addition to the above-mentioned works exhibiting shear-thinning characteristics in the studied flow, other research has yielded different findings. Anjaneyulu and Khakhar (1995) on Bingham plastics with glass beads, and Colafigli et al. (2009) on pseudoplastic behavior with silica particles, both reported lower wall shear stresses compared to this investigation.

4.3. Generalized Reynolds number

After developing a satisfactory model to describe the flow studied in this work (as shown in Fig. 5c), the friction factor can be calculated for the various conditions tested experimentally. Fig. 7 displays the values of the Fanning friction factor (10^0–10^5) against the generalized Reynolds number (10^{-4}–10^1) obtained for the proposed expression fitted to the current fluidized bed data [Eqs. (29) and (30)]. The relation that applies to a Newtonian laminar flow in circular pipes is also plotted for reference (dashed line). The rheological models proposed in this study shows minor deviations from this benchmark, confirming the assumption of laminar flow conditions with Reynolds numbers in the low laminar range (Metzner and Reed, 1955). This confirmation of the laminar profile indicates a velocity distribution across the transport channel, not a uniform mean velocity as assumed by the 1D convection-dispersion model (see Eq. (27)). Separating velocity distribution from dispersion requires accounting for the velocity profile of laminar flow, which is beyond the scope of this work.

Fig. 8 presents the Péclet number (defined as $Pe = u_S \cdot L/D_S$) plotted against the generalized Reynolds number for the cases investigated. The

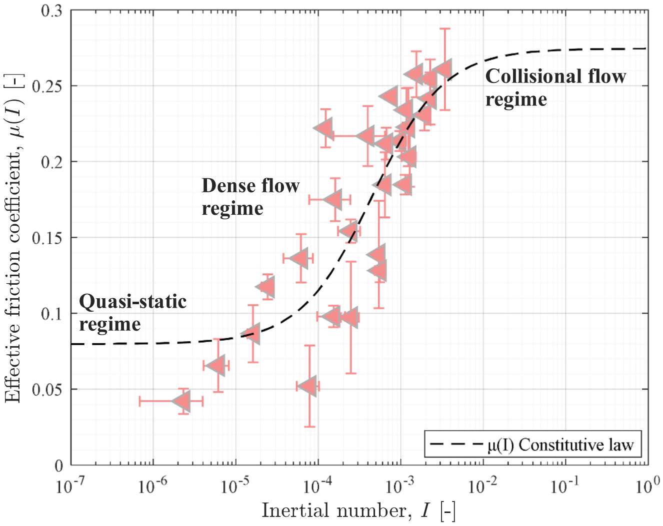

Fig. 9. Effective friction coefficient as a function of the inertial number. Experimentally derived values (markers) together with the fit to the constitutive law equation [Eq. (26)].

horizontal solids dispersion coefficient and solids velocity are derived from fitting the transient concentrations of the solids tracer to Eq. (27). These D_S-u_S data pairs are plotted in Kong et al. (2018). The Re^*-values are obtained using the correlation from the proposed model [Eqs. (29) and (30)]. An increasing trend between the two dimensionless parameters on the given log-log scale suggests that as viscous forces become less significant, convective transport becomes more dominant relative to dispersive transport (although the dispersion coefficient increases with solids velocity; see Fig. A.3). In industrial applications, this implies that at low Péclet numbers, a greater marginal energy input is required to increase velocity, whereas at high Péclet numbers, the same velocity increase requires less additional energy.

4.4. Granular flow regime

In addition, based on the theory of granular flow rheology, the effective friction coefficient can be calculated. Fig. 9 presents the effective friction coefficient [Eq. (24)] as a function of the inertial number [Eq. (25)], together with the fit to the $\mu(I)$ constitutive law (dashed line, $\mu_S = 0.08$, $\mu_2 = 0.28$, $I_0 = 4.5 \times 10^{-4}$), which yields $R^2 = 0.71$.

The experimental data encompasses an inertial number range of 10^{-6}–10^{-2}, while the effective friction coefficient ranges from 0.03–0.3. There is a positive correlation between the inertial number and the effective friction coefficient, indicating that the solids flow for all the investigated cases in this work occurs in the dense flow regime. While the constitutive law fit provides threshold values for the inertial number, indicating regime shifts, confirmation of these values requires a broader experimental window that is not feasible with the current experimental setup.

5. Conclusions

This study investigates frictional losses in horizontal fluidized solids flow using a down-scaled fluidized bed model, featuring a rectangular cross-sectional channel through which fluidized solids are conveyed. Measurements of horizontal pressure drop and solids flow rate were used to determine rheometric parameters. The solids velocity was extracted using the magnetic solids tracing (MST) method, complemented by in-bed pressure probes that sampled the pressure gradient. The effects of solids velocity, bed height, and channel width are considered. The results show that the normalized pressure gradient (0–1600 Pa/m) is directly proportional to the solids velocity (0–0.035 m/s). However, this gradient decreased with an increase in transport channel width, likely due to increased wall effects and boundary layer interactions in restricted geometries.

The analysis of the rheometric parameters showed that the horizontal flow of fluidized solids in a rectangular cross-section exhibits non-Newtonian behavior, more specifically shear-thinning. However, existing rheological models for non-Newtonian flow in non-circular geometries showed limited ability for describing the measured data, due to an underestimation of the impact of the geometric parameters. Instead, a power-law-based expression is proposed that can be fitted to the measurement data and better accounts for the channel width and bed height. The extraction of friction coefficients and Reynolds numbers using the proposed expression indicates that the solids flow remains within the laminar regime. The experiments covered the ranges of Reynolds numbers (10^{-4}–10^{1}), Fanning friction factors (10^{0}–10^{5}), wall shear stresses (5–55 Pa s), and wall shear rates (0.002–4.5 s^{-1}). It is demonstrated that an increased Re^*-number results in a nonlinear increase in the Pe-number, attributed to the dispersion coefficient also increasing with solids velocity. Lastly, based on granular flow theory, the analysis in terms of the $\mu(I)$ constitutive law indicates that the solids flow investigated occurs in the dense flow regime, with inertial numbers in the range of 10^{-6}–10^{-2} and corresponding effective friction coefficients in the range of 0.03–0.3.

CRediT authorship contribution statement

Munavara Farha: Writing – original draft, Validation, Methodology, Investigation, Formal analysis, Data curation. **Diana Carolina Guío-Pérez:** Writing – review & editing, Supervision, Conceptualization. **Filip Johnsson:** Writing – review & editing. **David Pallarès:** Writing – review & editing, Supervision, Funding acquisition, Conceptualization.

Declaration of competing interest

The authors declare the following financial interests/personal relationships which may be considered as potential competing interests:

David Pallares reports financial support was provided by Swedish Energy Agency. If there are other authors, they declare that they have no known competing financial interests or personal relationships that could have appeared to influence the work reported in this paper.

Acknowledgments

The authors acknowledge the financial support provided by the Swedish Energy Agency within the framework of project no. 51182-1 – *Thermochemical poly-generation in heat and power plants*. The contribution of RISE Sensor Systems is also acknowledged, which made possible the development of the Magnetic Solids Tracing system used in this work.

Appendix A

Fig. A.1 compares the RTD curves for the sections located between coils 1–2, 2–3, and 3–4 within the measurement zone, which are spaced equally, as depicted in Fig. 2a. These sections were analyzed using a deconvolution technique referenced in Farha et al. (2024), with input signals derived from coils 1, 2, and 3 for their respective slices. The resultant RTD curves overlap, indicating consistent mean residence times within a standard deviation of 1.478 s, thus supporting the hypothesis of a fully- developed flow.

This methodology extends to various conditions, showing entrance effects that are generally acceptable, though diminished at low solids conveying velocities. Nonetheless, the minor velocity variations observed across different segments have a negligible impact on the measured pressure drop gradient, affirming the assumption of a fully developed flow.

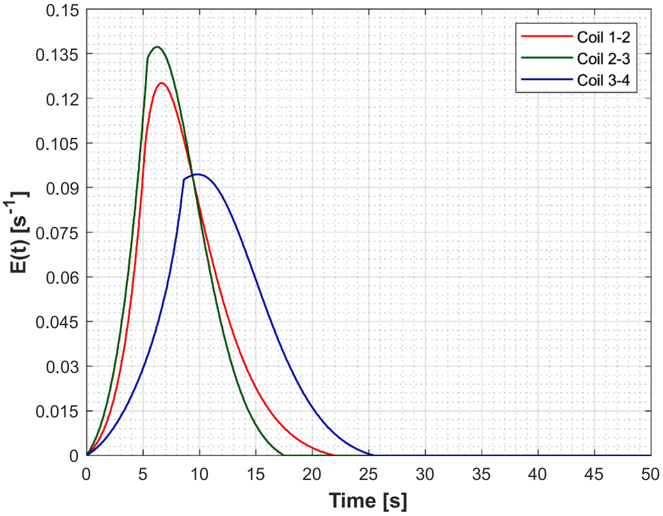

Fig. A.1. Overlapping RTD curves for the sections located between coils 1–2, 2–3, and 3–4, demonstrating consistent mean residence times and supporting the assumption of a fully developed flow. Conditions used for the experiment: $W = 0.07$ m, $H = 0.09$ m and $u_S = 0.012$ m/s.

Appendix B

The raw concentration signal profile from MST experiments is presented in Fig. A.2a. The concentration signals are extracted from four positions alongside the direction of the solids flow. As outlined in Section 3.1.3, solids velocity is determined by fitting concentration signals to the transient convection-dispersion equation [Eq. (27)], yielding two parameters: lateral solids velocity and solids dispersion coefficient. This study focuses solely on the velocity parameter, as dispersion effects are beyond the scope of the current work. Fig. A.2b illustrates the fitted concentration profiles alongside experimental data. A comprehensive discussion of the modeling procedure, including assumptions, boundary conditions, and error calculations, is provided in reference (Farha et al., 2024).

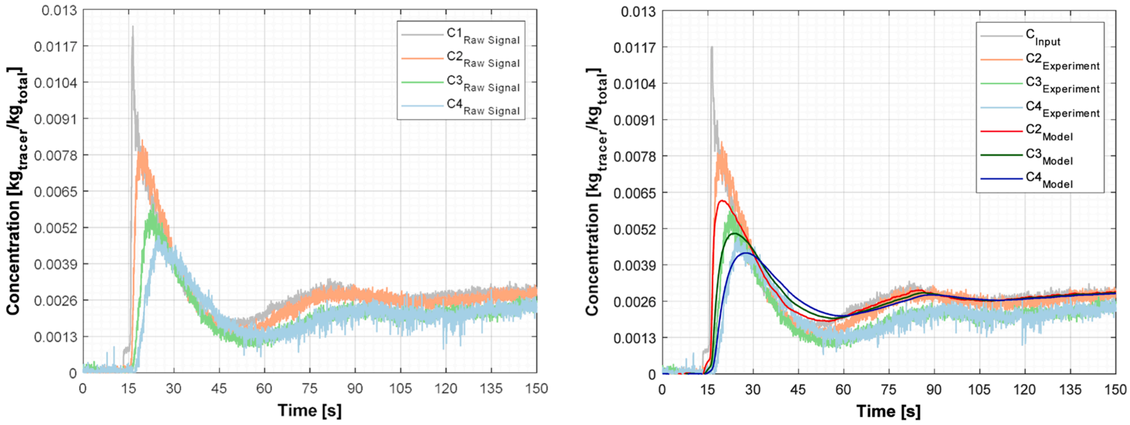

(a)

(b)

Fig. A.2. Estimation of solids velocity and dispersion coefficient based on model fitting using Eq. (27). ($FN_{TZ} = 3$, H = 0.10 m, W = 0.12 m, $u_S = 0.013$ m/s). (a) Transient profile of the measured tracer concentration. (b) Measured and modeled transient concentrations of the solids tracer.

Fig. A.3 presents the data pairs [solids horizontal velocity, solids horizontal dispersion coefficient] for each experimental condition, obtained after fitting the transient concentration data sampled by the coils to the convection-dispersion model [see Eq. (27)]. The highest dispersion rates are observed for the experiments with the widest channel geometries. This aligns with previous studies on fluidized beds, that have consistently demonstrated significantly higher dispersion coefficients in larger geometries (Sette et al., 2014), eventually reaching a saturation point (Liu and Chen, 2010). Furthermore, an increase in solids velocity leads to greater dispersive mixing, which has been observed previously (Farha et al., 2024) and this is hypothetically related to the enhanced mixing created by shear-induced flow structures, which become more significant at higher solids velocities. Lastly, in the case of the narrowest geometry, the dispersion coefficient remains saturated at a level that is independent of the solids velocity, which aligns with the previously mentioned observations regarding geometry-constrained dispersion rates.

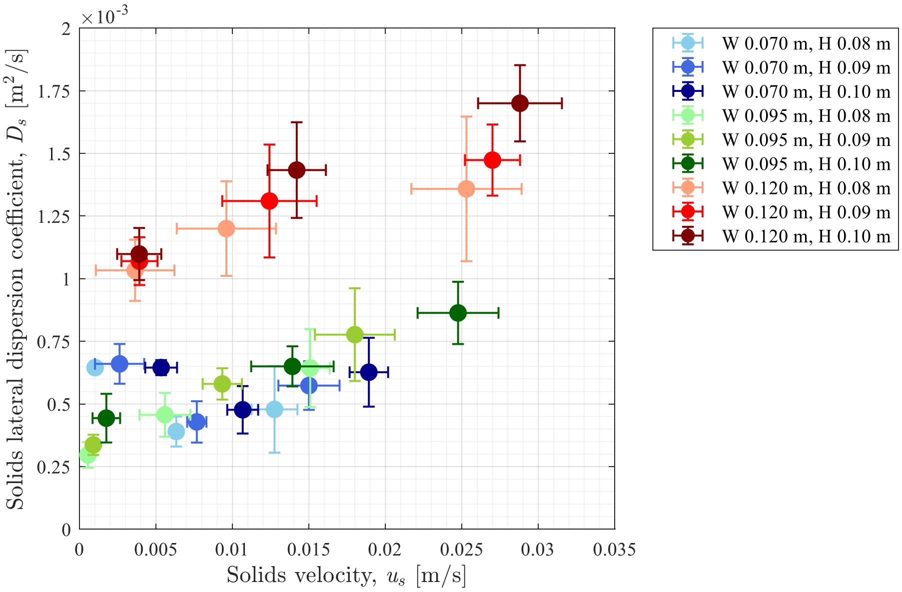

Fig. A.3. Solids horizontal velocity and dispersion coefficient from concentration data fitted to a convection-dispersion model.

Fig. A.4 presents the regression results, along with the main effects plots obtained for the solids velocity and solids lateral dispersion coefficient. Through regression analysis, the influences of operational factors on model-derived parameters were examined. *H* exerts the least impact on the response variables at 13–17 %. For the solids velocity, Q_{CZ} plays a greater role [64 %] than *W* [19 %]. Conversely, for the solids lateral dispersion coefficient, the influence of *W* [65 %] surpasses that of Q_{CZ} [22 %].

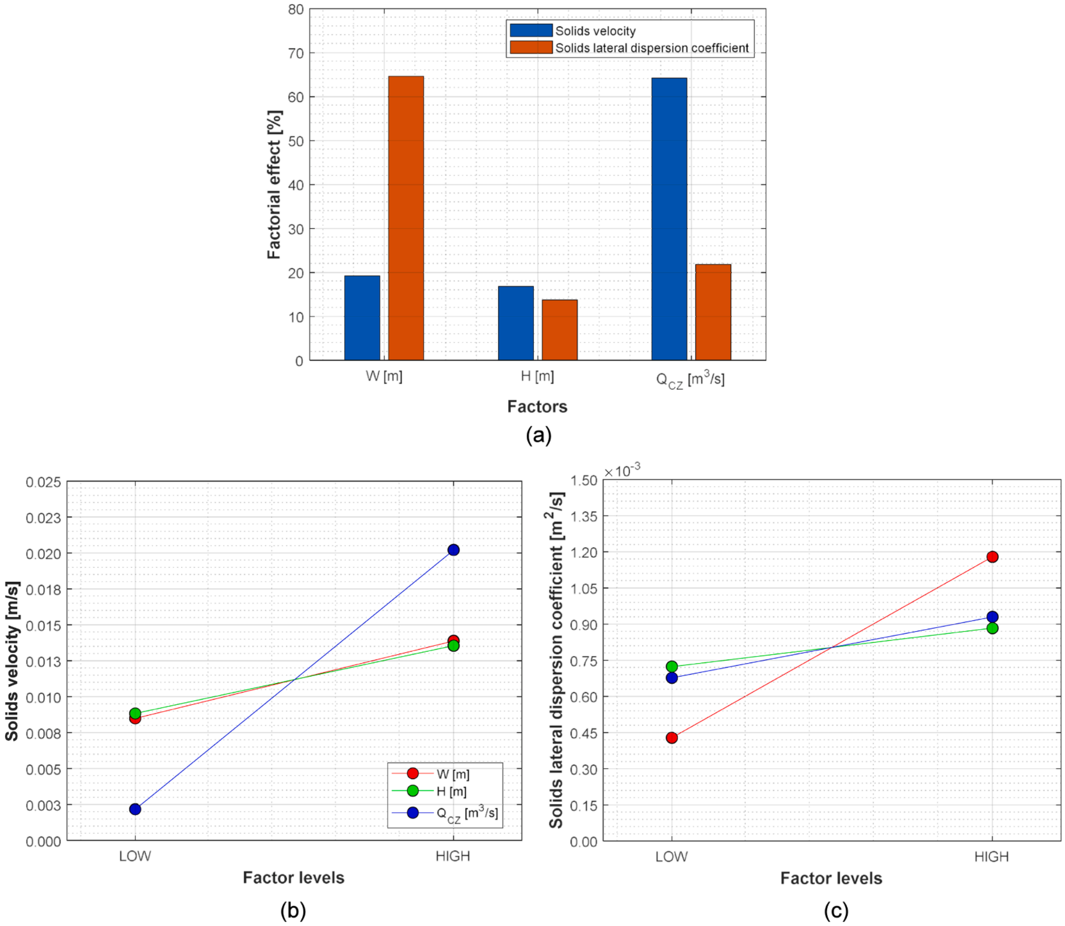

Fig. A.4. Regression model results. (a) Quantified contributions of determinant factors to the regression model. Main effects plots for: (b) the solids velocity; and (c) the solids lateral dispersion coefficient.

Appendix C

The fluid density is calculated using Eq. (7), where the bed voidage ‘ε_g’ is determined following the methodology described in (Farha et al., 2023). This approach involves in-bed pressure sampling at two vertically separated heights, $\Delta h = 0.04$ m. Fig. A.5 illustrates the pressure probe configuration used for bed voidage measurement. The pressure probes are mounted on a plexiglass plate, positioned at a designated section within the cold flow model to acquire vertical pressure drop data (ΔP). The module height is adjusted to three levels within the 0.06–0.08 m range above the perforated plate (Farha et al., 2023).

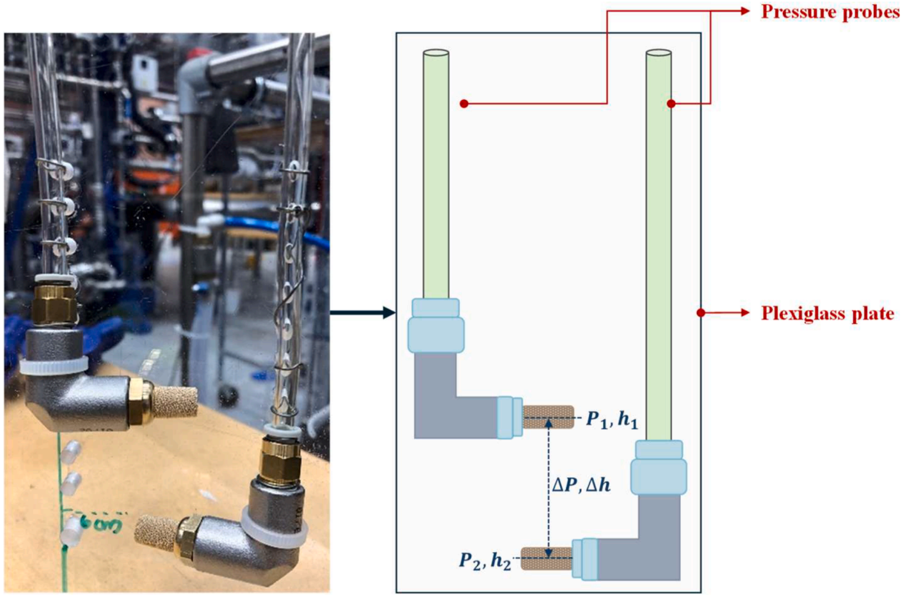

Fig. A.5. Pressure probe configuration for bed voidage measurement.

The obtained time series of fluid density is plotted in Fig. A.6, from which a time-averaged value of 3868.55 kg/m^3 is determined.

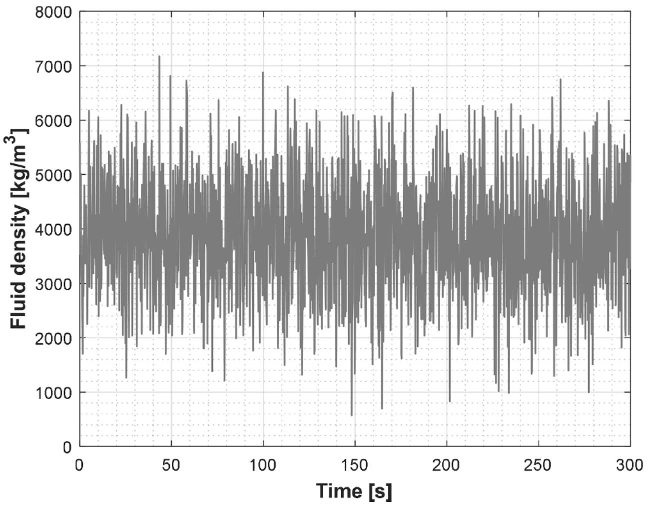

Fig. A.6. Time series of fluid density as calculated from pressure drop measurements.

Appendix D

Table A.1 lists the equations that were employed to calculate the wall shear stress for both the literature-based models and the current study.

Table A.1
Equations for wall shear stress: literature models and current study.

Rheological model	Model wall shear stress [Pa]
Model 1 (Kozicki et al., 1966; Kozicki and Tiu, 1967; Tiu et al., 1968; Kozicki and Tiu, 1971)	$\tau_w = K_{KT}\left[\frac{a+bn}{n}\right]^n\left[\frac{8u_S}{D_h}\right]^n$
Model 2 (Kostic and Hartnett, 1984; Ayas et al., 2019; Ayas et al., 2021)	$\tau_w = K_{KH}\xi\left[\frac{3n+1}{4n}\right]^n\left[\frac{8u_S}{D_h}\right]^n$
Model 3 (Delplace and Leuliet, 1995)	$\tau_w = K_{DL}\left[\frac{24n+\beta}{(24+\beta)n}\right]^n\left[\frac{\beta u_S}{D_h}\right]^n$
Current study	$\tau_w = K\left[C_W W_S + C_{H_b} H_{b,S}\right]^n\left[\frac{8u_S}{D_h}\right]^n$

Fig. A.7 presents a comparison of the wall shear stresses calculated by the three literature-based models and the current study, alongside the experimental data. The *y*-axis displays the model-calculated wall shear stress (Table A.1), while the *x*-axis represents the experimental wall shear stress derived from Eq. (3). Error bars reflect deviations in solids' velocity, based on three repetitions conducted for each case.

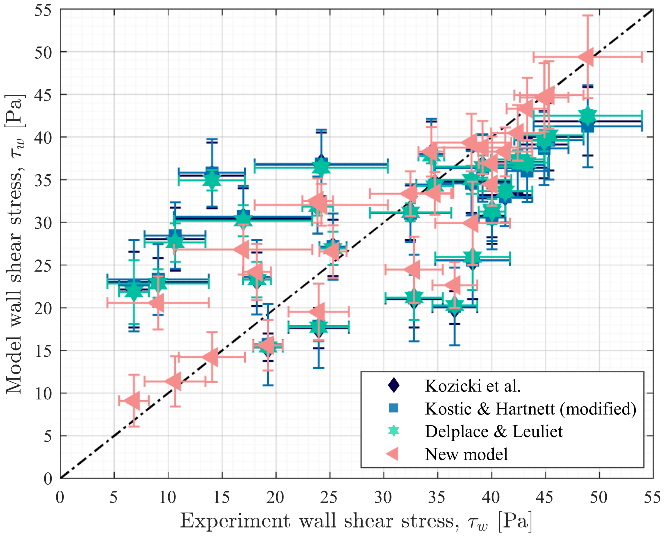

Fig. A.7. Comparison of the modeled and experimental wall shear stress values.

Fig. A.8 depicts the relationship between the wall shear stress (5–55 Pa) and the `true' wall shear rate (0.002–4.5 s^{-1}) as determined by the proposed model, indicating shear-thinning characteristics.

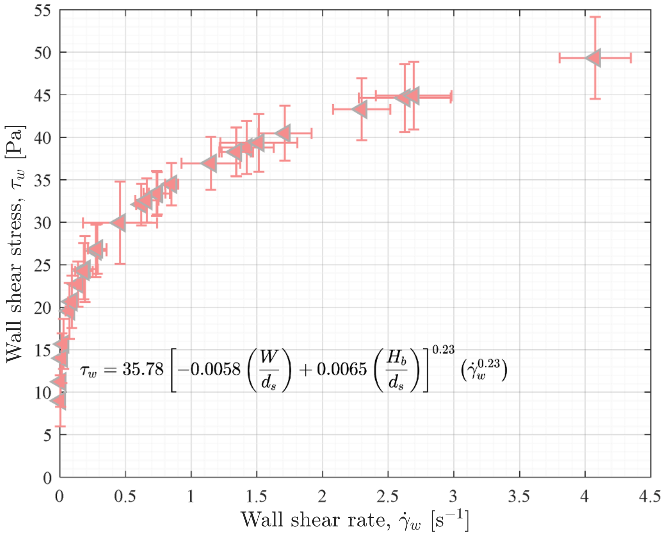

Fig. A.8. Wall shear stress vs. wall shear rate profile for the proposed model.

Apparent viscosity is a measure of a non-Newtonian fluid's resistance to flow under given conditions, reflecting how its viscosity changes with the rate of shear strain. The apparent viscosity can be calculated from:

$$\eta(\dot{\gamma}_w) = \frac{\tau_w}{\dot{\gamma}_w} \tag{A.4}$$

Fig. A.9 depicts the apparent viscosity profile as a function of wall shear strain. Observed viscosities span a range of 10–7000 Pa s, corresponding to wall shear strain rates in the range of 10^{-3}–4.5 s^{-1}. Across all three channel widths, there is a discernible trend towards decreasing viscosity with increasing wall shear strain.

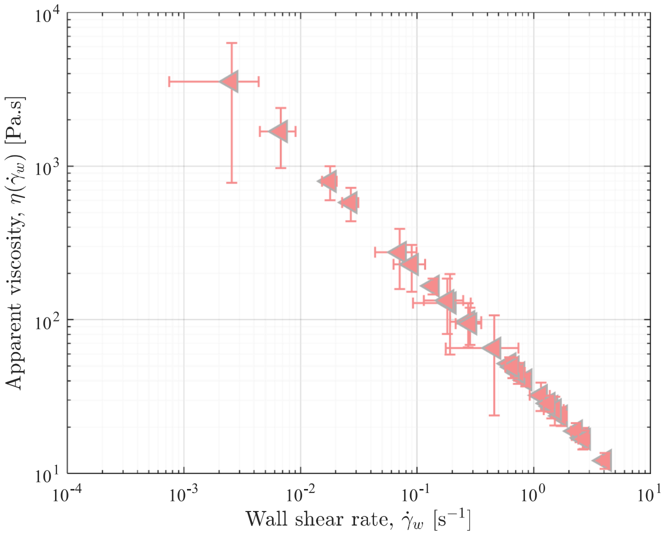

Fig. A.9. Apparent viscosity profile versus wall shear strain.

Appendix E

In the present work, the calculation of the hydraulic diameter for open channel flow, as defined in Eq. (2), excludes the gas distributor plate based on experimental observations (see the discussion related to Fig. 3). For comparison purposes, this appendix presents results from the case where the bottom plate is included, yielding $D_h = 4\frac{WH_b}{W+2H_b}$. Fig. A.10 presents the wall shear stress versus wall shear rate profile for this modified calculation.

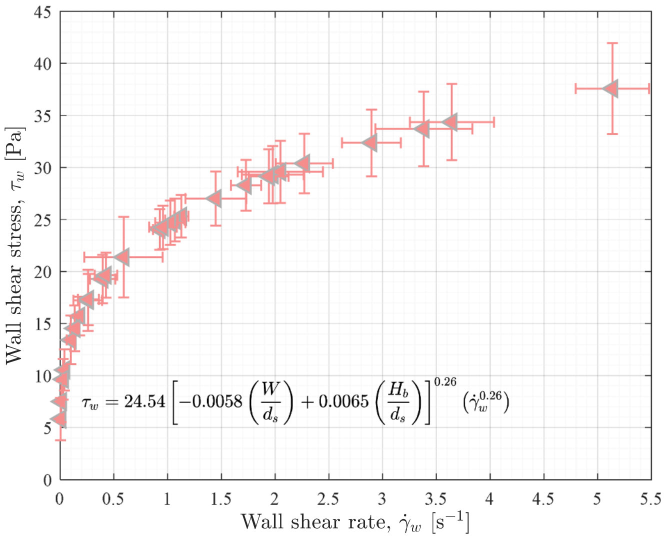

Fig. A.10. Wall shear stress versus wall shear rate profile for the hydraulic diameter calculation including the perforated plate.

When the gas distributor plate is included in the wetted perimeter calculation, the wall shear stress decreases by approximately 17.91 % at low shear rates and 23.85 % at high shear rates compared to when it is excluded (see Fig. A.8). This reduction is attributed to the increased effective perimeter, which distributes shear forces over a larger surface area. Excluding the bottom plate in this work is justified by the impact of bed height and channel width on horizontal pressure drop at equivalent solids velocities (see Fig. 3). Rather than reducing pressure drop due to a decrease in contact perimeter, a narrower channel width instead increases pressure drop, indicating the dominant role of shear interactions with the vertical walls. Therefore, the gas-injected bottom surface contributes minimally to shear resistance due to its lubrication effect.

Data availability

Data will be made available on request.

References

Anjaneyulu, P., Khakhar, D.V., 1995. Rheology of a gas-fluidized bed. Powder Technol. 83, 29–34.

Aronsson, J., Pallarès, D., Lyngfelt, A., 2017. Modeling and scale analysis of gaseous fuel reactors in chemical looping combustion systems. Particuology 35, 31–41. https://doi.org/10.1016/j.partic.2017.02.007.

Ayas, M., Skocilas, J., Jirout, T., 2019. A practical method for predicting the friction factor of power-law fluids in a rectangular duct. Chem. Eng. Commun. 206, 1310–1316. https://doi.org/10.1080/00986445.2018.1557153.

Ayas, M., Skocilas, J., Jirout, T., 2021. Friction factor of shear thinning fluids in non-circular ducts—A simplified approach for rapid engineering calculation. Chem. Eng. Commun. 208, 1209–1217. https://doi.org/10.1080/00986445.2020.1770232.

Bakhtiyarov, S., Overfelt, R., Reddy, S., 1996. Study of the apparent viscosity of fluidized sand. In: Proceedings in Rheology and Fluid Mechanics of Nonlinear Materials. ASME International Mechanical Engineering Congress. United Engineering Center, New York, pp. 243–249. https://doi.org/10.1115/IMECE1996-0248.

Basu, P., 2006. Combustion and Gasification in Fluidized Beds. CRC Press.

Bhattad, A., 2023. Review on viscosity measurement: devices, methods and models. J. Therm. Anal. Calorim. 148, 6527–6543. https://doi.org/10.1007/s10973-023-12214-0.

Bird, R.B., Stewart, W.E., Lightfoot, E.N., 2007. Transport Phenomena, second ed. Wiley https://search.ebscohost.com/login.aspx?direct=true&db=cat09075a&AN=clpc.oai.edge.chalmers.folio.ebsco.com.fs00001000.b778234a.6a2c.4c76.892c.2edfbf935c60&site=eds-live&scope=site&authtype=guest&custid=s3911979&groupid=main&profile=eds.

Bouillard, J., Henry, F., Marchal, P., 2014. Rheology of powders and nanopowders through the use of a Couette four-bladed vane rheometer: flowability, cohesion energy, agglomerates and dustiness. J. Nanopart. Res. 16. https://doi.org/10.1007/s11051-014-2558-0.

Breault, R.W., Mathur, V.K., 1989. High-velocity fluidized bed hydrodynamic modeling. 1. Fundamental studies of pressure drop. Ind. Eng. Chem. Res. 28, 684–688. https://pubs.acs.org/sharingguidelines.

Burger, J., Haldenwang, R., Alderman, N., 2010. Friction factor-Reynolds number relationship for laminar flow of non-Newtonian fluids in open channels of different cross-sectional shapes. Chem. Eng. Sci. 65, 3549–3556. https://doi.org/10.1016/j.ces.2010.02.040.

Burger, J.H., Haldenwang, R., Alderman, N.J., 2015. Laminar and turbulent flow of non-Newtonian fluids in open channels for different cross-sectional shapes. J. Hydraul. Eng. 141. https://doi.org/10.1061/(asce)hy.1943-7900.0000968.

C.S. Campbell, D.G. Wang, A particle pressure transducer suitable for use in gas-fluidized, 1990.

Campbell, C.S., Wang, D.G., 1991. Particle pressures in gas-fluidized beds. J. Fluid Mech. 227, 495–508. https://doi.org/10.1017/S0022112091000216.

Capes, C.E., Nakamura, K., 1973. Vertical pneumatic conveying: an experimental study with particles in the intermediate and turbulent flow regimes. Can. J. Chem. Eng. 51, 31–38. https://doi.org/10.1002/cjce.5450510106.

Chen, K., Bachmann, P., Bück, A., Jacob, M., Tsotsas, E., 2017. Experimental study and modeling of particle drying in a continuously-operated horizontal fluidized bed. Particuology 34, 134–146. https://doi.org/10.1016/j.partic.2017.02.003.

Chevoir, F., Roux, J.-N., da Cruz, F., Rognon, P.G., Koval, G., 2009. Friction law in dense granular flows. Powder Technol. 190, 264–268. https://doi.org/10.1016/j.powtec.2008.04.061.

Chhabra, R.P., 2007. Bubbles, Drops, and Particles in Non-Newtonian Fluids, second ed. CRC Taylor & Francis https://search.ebscohost.com/login.aspx?direct=true&db=cat07472a&AN=clec.ybp15915688&site=eds-live&scope=site&authtype=guest&custid=s3911979&groupid=main&profile=eds.

Chhabra, R.P., Comiti, J., Machač, I., 2001. Flow of non-Newtonian fluids in fixed and fluidised beds. Chem. Eng. Sci. 56, 1–27. https://doi.org/10.1016/S0009-2509(00)00207-4.

Chhabra, R.P., Richardson, J.F., 2008. Non-Newtonian Flow and Applied Rheology: Engineering Applications, second ed. Butterworth-Heinemann https://search.ebscohost.com/login.aspx?direct=true&db=cat09075a&AN=clpc.oai.edge.chalmers.folio.ebsco.com.fs00001000.0bcae914.ea00.4faa.9087.6614c1939e2e&site=eds-live&scope=site&authtype=guest&custid=s3911979&groupid=main&profile=eds.

Chow, V.T., 1959. Open Channel Hydraulics. McGraw-Hill, New York.

Colafigli, A., Mazzei, L., Lettieri, P., Gibilaro, L., 2009. Apparent viscosity measurements in a homogeneous gas-fluidized bed. Chem. Eng. Sci. 64, 144–152. https://doi.org/10.1016/j.ces.2008.08.036.

Coussot, P., 2005. Rheometry of Pastes, Suspensions, and Granular Materials: Applications in Industry and Environment. Wiley. https://search.ebscohost.com/login.aspx?direct=true&db=cat09075a&AN=clpc.oai.edge.chalmers.folio.ebsco.com.fs00001000.60becc48.ca9b.4af3.bbc5.aa4210ab8ae8&site=eds-live&scope=site&authtype=guest&custid=s3911979&groupid=main&profile=eds.

da Cruz, F., Emam, S., Prochnow, M., Roux, J.-N., Chevoir, F., 2005. Rheophysics of dense granular materials: discrete simulation of plane shear flows. Phys. Rev. E 72, 21309. https://doi.org/10.1103/PhysRevE.72.021309.

Delplace, F., Leuliet, J.C., 1995. Generalized Reynolds number for the flow of power law fluids in cylindrical ducts of arbitrary cross. Trends. Pharmacol. Sci. https://api.semanticscholar.org/CorpusID:78796951.

Djerf, T., Pallarès, D., Johnsson, F., 2021. Solids flow patterns in large-scale circulating fluidised bed boilers: experimental evaluation under fluid-dynamically down-scaled conditions. Chem. Eng. Sci. 231, 116309. https://doi.org/10.1016/j.ces.2020.116309.

Farha, M., Guío-Pérez, D.C., Aronsson, J., Johnsson, F., Pallarès, D., 2023. Assessment of experimental methods for measurements of the horizontal flow of fluidized solids under bubbling conditions. Fuel 348, 128515. https://doi.org/10.1016/j.fuel.2023.128515.

Farha, M., Guío-Pérez, D.C., Johnsson, F., Pallarès, D., 2024. Characterization of the solids crossflow in a bubbling fluidized bed. Powder Technol., 119967 https://doi.org/10.1016/j.powtec.2024.119967.

Garić, R.V., Grbavčić, Ž.B., Jovanović, S.Dj., 1995. Hydrodynamic modeling of vertical non-accelerating gas-solids flow. Powder Technol. 84, 65–74.

Geldart, D., 1973. Types of gas fluidization. Powder Technol. 7, 285–292. https://doi.org/10.1016/0032-5910(73)80037-3.

Glicksman, L.R., Hyre, M., Woloshun, K., 1993. Simplified scaling relationships for fluidized beds. Powder Technol. 77, 177–199. https://doi.org/10.1016/0032-5910(93)80055-F.

Grace, J.R., Leckner, B., Zhu, J., Cheng, Y., 2006. Fluidized beds. Multiph. Flow Handb. 5, 1–93.

Guío-Pérez, D.C., Köhler, A., Prati, A., Pallarès, D., Johnsson, F., 2023. Effective drag on spheres immersed in a fluidized bed at minimum fluidization—Influence of bulk solids properties. Can. J. Chem. Eng. 101, 210–226. https://doi.org/10.1002/cjce.24575.

Hariu, O.H., Molstad, M.C., 1949. Pressure drop in vertical tubes in transport of solids by gases. Ind. Eng. Chem. 41 (6), 1148–1160. https://doi.org/10.1021/ie50474a008.

Jones, J.H., Braun, W.G., Daubert, T.E., Allendorf, H.D., 1967. Estimation of pressure drop for vertical pneumatic transport of solids. AIChE J. 13, 608–611. https://doi.org/10.1002/aic.690130338.

Jones, M.G., Williams, K.C., 2003. Solids friction factors for fluidized dense-phase conveying. Part. Sci. Technol. 21, 45–56. https://doi.org/10.1080/02726350307495.

Jop, P., Forterre, Y., Pouliquen, O., 2006. A constitutive law for dense granular flows. Nature 441, 727–730. https://doi.org/10.1038/nature04801.

Kmieć, A., Mielczarski, S., Pajakowska, J., 1978. An experimental study on hydrodynamics of a system in a pneumatic flash dryer. Powder. Technol. 20, 67–74.

Köhler, A., Guío-Pérez, D.C., Prati, A., Larcher, M., Pallarès, D., 2021. Rheological effects of a gas fluidized bed emulsion on falling and rising spheres. Powder Technol. 393, 510–518. https://doi.org/10.1016/j.powtec.2021.07.064.

Kong, W., Wang, B., Baeyens, J., Li, S., Ke, H., Tan, T., Zhang, H., 2018. Solids mixing in a shallow cross-flow bubbling fluidized bed. Chem. Eng. Sci. 187, 213–222. https://doi.org/10.1016/j.ces.2018.04.073.

Konno, H., Saito, S., 1969. Pneumatic conveying of solids through straight pipes. J. Chem. Eng. Jpn. 2.

Kostic, M.M., Hartnett, J.P., 1984. Predicting turbulent friction factors of non-Newtonian fluids in noncircular ducts. Int. Commun. Heat Mass Transf. 11, 345–352. https://api.semanticscholar.org/CorpusID:120144713.

Kottlan, A., Schuetz, D., Radl, S., 2018. Rheological investigations on free-flowing and cohesive powders in different states of aeration, using a ball measuring system. Powder Technol. 338, 783–794. https://doi.org/10.1016/j.powtec.2018.07.048.

Kozicki, W., Chou, C.H., Tiu, C., 1966. Non-Newtonian Flow in Ducts of Arbitrary Cross-Sectional Shape. Pergamon Press Ltd.

Kozicki, W., Tiu, C., 1967. Non-Newtonian flow through open channels. Can. J. Chem. Eng. 45, 127–134. https://doi.org/10.1002/cjce.5450450302.

Kozicki, W., Tiu, C., 1971. Improved parametric characterization of flow geometries. Can. J. Chem. Eng. 49, 562–569. https://doi.org/10.1002/cjce.5450490503.

Kunii, D., Levenspiel, O., 1991. Fluidization Engineering, second ed. Butterworth-Heinemann https://search.ebscohost.com/login.aspx?direct=true&db=cat09075a&AN=clpc.oai.edge.chalmers.folio.ebsco.com.fs00001000.cfe5a823.1497.4690.b602.bbd293482377&site=eds-live&scope=site&authtype=guest&custid=s3911979&groupid=main&profile=eds.

Kunii, D., Levenspiel, O., 1991. Fluidization Engineering. Butterworth-Heinemann, Boston.

Lech, M., 2001. Mass flow rate measurement in vertical pneumatic conveying of solid. Powder Technol. 114, 55–58. www.elsevier.comrlocaterpowtec.

Levenspiel, O., 2012. Tracer Technology. Springer New York. https://doi.org/10.1007/978-1-4419-8074-8.

Liu, D., Chen, X., 2010. Lateral solids dispersion coefficient in large-scale fluidized beds. Combust. Flame 157, 2116–2124. https://doi.org/10.1016/j.combustflame.2010.04.020.

Mabrouk, R., Chaouki, J., Guy, C., 2008. Wall surface effects on particle-wall friction factor in upward gas-solid flows. Powder Technol. 186, 80–88. https://doi.org/10.1016/j.powtec.2007.11.009.

Metzner, A.B., Reed, J.C., 1955. Flow of non-Newtonian fluids—Correlation of the laminar, transition, and turbulent-flow regions. AIChE J. 1, 434–440. https://doi.org/10.1002/aic.690010409.

MiDi, G.D.R., 2004. On dense granular flows. Eur. Phys. J. E 14, 341–365. https://doi.org/10.1140/epje/i2003-10153-0.

Mooney, M., 1931. Explicit formulas for slip and fluidity. J. Rheol. (N. Y. N. Y.) 2, 210–222. https://doi.org/10.1122/1.2116364.

Murakami, T., Xu, G., Suda, T., Matsuzawa, Y., Tani, H., Fujimori, T., 2007. Some process fundamentals of biomass gasification in dual fluidized bed. Fuel 86, 244–255. https://doi.org/10.1016/j.fuel.2006.05.025.

Özbelge, T.A., 1984. Solids friction factor correlation for vertical upward pneumatic conveyings. Int. J. Multiph. Flow 10, 459–465.

Parvathaneni, S., Kodukula, B., Andrade, M.W., 2024. Iron-ore reduction in fluidized beds: review of commercial technologies, status, and challenges. Ind. Eng. Chem. Res. 63, 18724–18733. https://doi.org/10.1021/acs.iecr.4c02282.

Pawar, D.S., Surwase, R.K., Bhamare, S.B., Pagar, S.P., 2020. Fluidized bed granulation: a promising technique. Int. J. Pharm. Sci. Rev. Res. 64, 133–140. https://doi.org/10.47583/ijpsrr.2020.v64i02.022.

B. Rabinowitsch, Über die viskosität und elastizität von Solen, 145A (1929) 1–26. doi:10.1515/zpch-1929-14502.

Ramli, W., Daud, W., 2007. A cross-flow model for continuous plug flow fluidized-bed cross-flow dryers. Dry Technol. 25, 1229–1235. https://doi.org/10.1080/07373930701438618.

Rautiainen, A., Sarkomaa, P., 1998. Solids friction factors in upward, lean gas-solids flows. Powder Technol. 95, 25–35.

Sette, E., Pallarès, D., Johnsson, F., 2014. Experimental quantification of lateral mixing of fuels in fluid-dynamically down-scaled bubbling fluidized beds. Appl. Energy 136, 671–681. https://doi.org/10.1016/j.apenergy.2014.09.075.

Straub, L.G., Silberman, E., Nelson, H.C., 1958. Open-channel flow at small Reynolds numbers. Trans. Am. Soc. Civ. Eng. 123, 685–706. https://doi.org/10.1061/TACEAT.0007627.

Tiu, C., Kozicki, W., Phung, T.Q., 1968. Geometric parameters for some flow channels. Can. J. Chem. Eng. 46, 389–393. https://doi.org/10.1002/cjce.5450460601.

Versteeg, H.K., Malalasekera, W., 2007. An Introduction to Computational Fluid Dynamics: The Finite Volume Method, second ed. Pearson Prentice Hall https://search.ebscohost.com/login.aspx?direct=true&db=cat09075a&AN=clpc.oai.edge.chalmers.folio.ebsco.com.fs00001000.5b591ae2.cbff.4ea1.afce.1c0202409073&site=eds-live&scope=site&authtype=guest&custid=s3911979&groupid=main&profile=eds.

Wanjari, A.N., Thorat, B.N., Baker, C.G.J., Mujumdar, A.S., 2006. Design and modeling of plug flow fluid bed dryers. Dry Technol. 24, 147–157. https://doi.org/10.1080/07373930600558946.

Winter, F., Schratzer, B., 2013. 23—Applications of fluidized bed technology in processes other than combustion and gasification. In: Scala, F. (Ed.), Fluidized Bed Technologies for Near-Zero Emission Combustion and Gasification. Woodhead Publishing, pp. 1005–1033. https://doi.org/10.1533/9780857098801.5.1005.

Yahia, L.A.A., Piepke, T.M., Barrett, R., Ozel, A., Ocone, R., 2020. Development of a virtual Couette rheometer for aerated granular material. AIChE J. 66. https://doi.org/10.1002/aic.16945.

Yates, J.G., 1983. Fundamentals of Fluidized Bed Chemical Processes. Butterworth Publishers, Stoneham, MA, United States. https://www.osti.gov/biblio/7129060.

Yin, C., Rosendahl, L.A., Kær, S.K., 2008. Grate-firing of biomass for heat and power production. Prog. Energy Combust. Sci. 34, 725–754. https://doi.org/10.1016/j.pecs.2008.05.002.

Zhang, Y., Abatzoglou, N., 2022. Modelling of continuous drying of heat-sensitive pharmaceutical granules in a horizontal fluidised bed dryer combined with a screw conveyor at steady state. Chem. Eng. Sci. 255, 117678. https://doi.org/10.1016/j.ces.2022.117678.